SAPIENZA
UNIVERSITÀ DI ROMA

Innovative strategies to streamline continuous gravitational-wave candidates in the advanced LIGO-Virgo detector era

Scuola di Dottorato in Fisica

Dottorato di Ricerca in Fisica – XXXII Ciclo

Candidate

Giuseppe Intini

ID number 1227552

Thesis Advisor

Prof. Paola Leaci

2020

Thesis defended on 30 November 2020
in front of a Board of Examiners composed by:

Prof. Paolo De Bernardis (chairman)

Prof. Vincenzo Canale

Prof. Fedele Lizzi

Innovative strategies to streamline continuous gravitational-wave candidates in the advanced LIGO-Virgo detector era

Ph.D. thesis. Sapienza – University of Rome

This thesis has been typeset by LaTeX and the Sapthesis class.

Version: December 6, 2020

Author's email: intinigiuseppe@gmail.com

Abstract

The goal of the LIGO-Virgo community is the gravitational-wave (GW) search and the consequent achievement of a deep knowledge of the universe. Although great results have been already obtained by detecting coalescing compact objects (such as binary Black Holes and even a Binary Neutron star), a lot of work remains still to be done, especially for what concerns Continuous GWs (CWs). Those signals, due to their long duration, have a central role in the study of the Universe, but are fainter than the signals we have detected so far. This Ph.D. thesis is focused on finding innovative strategies to improve CW searches in the advanced LIGO-Virgo detector era [1, 7].

The most accredited CW sources are non-axisymmetric rotating neutron stars. In general, there are four different approaches to study these signals: targeted, narrow band, directed and all-sky searches. The targeted search is a search where we assume to know all information on the source (sky position, spin frequency and its derivatives). The narrow band search widens the portion of frequency and its derivatives, working on an interval centered at the known information. The directed search considers stars whose sky position is known, but no information on the star spin frequency and derivatives is provided. In these cases, we can use a matched-filter technique. In fact, having at most two parameters to span, it is possible to perform a matched-filter search changing the parameters at a reasonable computational cost. In all-sky searches we are interested to look for CWs coming from unknown sources. In this case we cannot use the matched-filter technique due to the large size of the parameter space that must be spanned. Hence, we need to use hierarchical searches, such as the FrequencyHough algorithm, which is the core of this Ph.D. work. In the FrequencyHough search[12], the number of candidates obtained from the procedure is too high to be followed up, so it is necessary to rank them and deeply follow up only the most significant ones. However, it is not trivial to apply the procedure over a big portion of the frequencies we need to study as the computational cost grows linearly with frequency.

Our goal is to identify CWs in the LIGO-Virgo data and estimate their parameters (sky position, frequency and first time derivative). For this purpose, we have analyzed candidates returned by the FrequencyHough pipeline to find a method to filter out the bulk of them. We have found out that any (injected) signal creates, besides a candidate with the parameters closest to those of the injected CW signal, a set of byproducts for which a small error in one of the parameters is compensated by small errors on the others according to some rules. Those byproducts have a detection statistic which tends to be higher than that for the background-noise candidates. Hence, the rules of error compensation create a correlation in the parameter space that links the sky position to the frequency and its time derivative.Once we identified those rules, and the patterns that they create, we have developed a veto procedure that uses those patterns to identify the presence of a CW signal. If we don't have a pattern of candidates in the parameter space, it is unlikely that we will have a signal strong enough to be successfully detected in the follow up step. The innovative procedure we developed consists of computing two additional Hough transforms on the set of initial candidates, checking whether any correlation is present in the search parameter space and, alternatively, removing the candidates. The overall procedure removes about 50% of the false candidates (without excluding those related to the injected signals).

Another aspect covered by the current Ph.D. thesis consists in trying to find alternative polarizations with respect to those that are foreseen by the General Relativity (GR) [16]. We have studied how deep potential nonGR components of GWs can be detected by the current *5vector* targeted pipeline, and proposed an *ad hoc* solution for their detection with this pipeline.

Contents

Chapter 1

Introduction

In this chapter we will summarize the gravitational waves (GWs), focusing on the type of signal we expected and the detection techniques we used for the continuous GWs (CW for Continuous Waves).

Theorized by Einstein in 1916 [16], GWs are ripples of the spacetime which travels at the speed of light and are mainly produced by asymmetric masses acceleration. In the last century there have been many attempts to modify the General Relativity theory (especially in order to make it compatible with quantum field theory), and these attempts impact on GWs theoretical speed and, consequently, on its valid polarizations. Anyway, in this chapter we will focus on General Relativity theory which, ut least up to now, appears to be the more likely according to directed and undirected tests.

The General Relativity has been developed in order to make gravity compatible with the relativistic theory. Starting from the equivalence principle[1], Einstein states that a gravitational field is not a distance-based force but the effect of a spacetime curvature due to the mass presence. Such a principle has been formalized with the so-called Einstein Equations

$$G_{\mu\nu} = R_{\mu\nu} - \frac{1}{2} g_{\mu\nu} R = \chi T_{\mu\nu}, \qquad \chi = \frac{8\pi G}{c^4}, \tag{1.1}$$

where $R_{\mu\nu} = g^{\alpha\beta} R_{\mu\nu\alpha\beta}$ is the Riemann Tensor contraction and $R = g^{\mu\nu} R_{\mu\nu}$ is the spacetime curvature scalar; $g_{\mu\nu}$ the metric tensor on the space-time; $T_{\mu\nu}$ the Stress-Energy tensor describing the matter distribution; G is the universal gravitational constant and c is the speed of light.

The (1.1) are non-linear differential equations which already contains the gravitational field propagation as a wave. The strong non-linearity makes it impossible to exactly solve the propagation equations (while stationary solutions have been found). We can find approximate solution when the time-dependent part of the metric tensor is much smaller than the non-null components of the tensor itself.

[1] The strong equivalence principle state in an arbitrary gravitational field, at any given spacetime point, we can choose a locally inertial reference frame such that, in a sufficiently small region surrounding that point, all physical laws take the same form they would take in absence of gravity, namely the form prescribed by Special Relativity [16, 31]).

The standard case is a GW propagating in the Minkowskian space [2]with small time-varying perturbations ($g_{\mu\nu} = \eta_{\mu\nu} + h_{\mu\nu}$). It is easy to obtain [31] that the small perturbations evolve accordingly to the wave equations

$$\Box \overline{h}_{\mu\nu} = -\frac{16\pi G}{c^4} T_{\mu\nu} \tag{1.3a}$$

$$\frac{\partial \overline{h}^{\mu}_{\lambda}}{\partial x^{\mu}} = 0, \tag{1.3b}$$

where $\overline{h}_{\mu\nu} \equiv h_{\mu\nu} + \frac{1}{2}\eta_{\mu\nu} h^{\lambda}{}_{\lambda}$. Note that the right part of the equation (1.3a) is 0 in the vacuum.

Using the solutions (1.3a) and (1.3b), we obtain the waveform inside the source:

$$\overline{h}^{\mu 0} = 0 \qquad \mu = 0,1,2,3 \tag{1.4a}$$

$$\overline{h}^{ik}(t,r) = \frac{2G}{c^4, r} \cdot \left[\frac{\mathrm{d}^2}{\mathrm{d}t^2} \frac{1}{c^2} \int_V T_{00}(r - ct, x^n) x^i x^k \mathrm{d}^3 x \right] \qquad i,k,n = 1,2,3. \tag{1.4b}$$

The integrated part in the equation (1.4b) is the mass-energy value of the stress-energy tensor times the two coordinates x^i e x^k. This term is the i-th, k-th term of the quadrupole momentum [31].

The symmetry of the system ($h^{ij} = h^{ji}$) shows us that we have 6 degrees of freedom, but we can still set 4 gauge conditions that leave 2 non-null degrees of freedom. We use them to select the so-called Transverse-Traceless gauge, where all the components which insist on the wave motion axis are set to 0 and the same is done for the trace. The result has the typical propagating wave form (that is proportional to $\cos(\omega t - \kappa x)$). Thus, if we define the **z** axis as the wave propagating direction, the wave has the form

$$h^{TT}_{\mu\nu} = \begin{pmatrix} 0 & 0 & 0 & 0 \\ 0 & h_+ & h_\times & 0 \\ 0 & h_\times & -h_+ & 0 \\ 0 & 0 & 0 & 0 \end{pmatrix} \cdot \cos(\omega t - \kappa z), \tag{1.5}$$

with ω e κ respectively the angular frequency and the absolute value of the wave (three-)vector[3].

The (1.5) shows us that the two degrees of freedom are the two GW's polarizations which differently modify the distance between two points. Using the four-distance, defined as

$$\mathrm{d}s^2 = g^{\mu\nu} \mathrm{d}x_\mu \mathrm{d}x_\nu, \tag{1.6}$$

it is possible to obtain GW effect on the distances. From (1.6), we observe that the distance modification given by a GW is proportional to the distance itself.

[2]That is a flat spacetime, with a metric

$$\eta_{\mu\nu} = \begin{pmatrix} -1 & 0 & 0 & 0 \\ 0 & 1 & 0 & 0 \\ 0 & 0 & 1 & 0 \\ 0 & 0 & 0 & 1 \end{pmatrix}. \tag{1.2}$$

[3]We also obtain from (1.3b) that, given $\kappa_\mu = (\omega, \vec{\kappa})$, $k_\mu k^\mu = 0$.

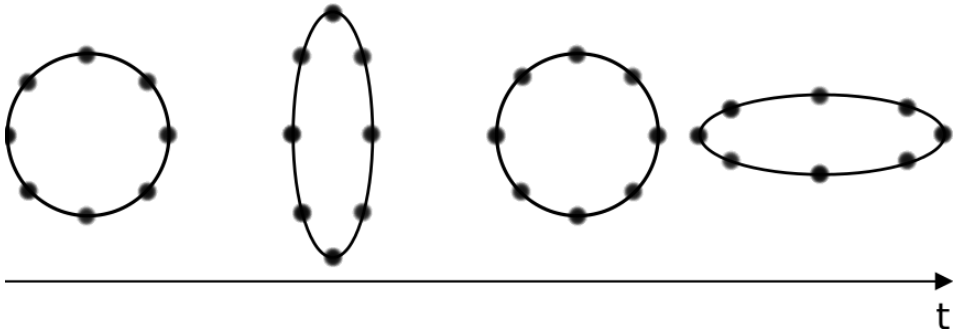

(a) + polarized wave effect

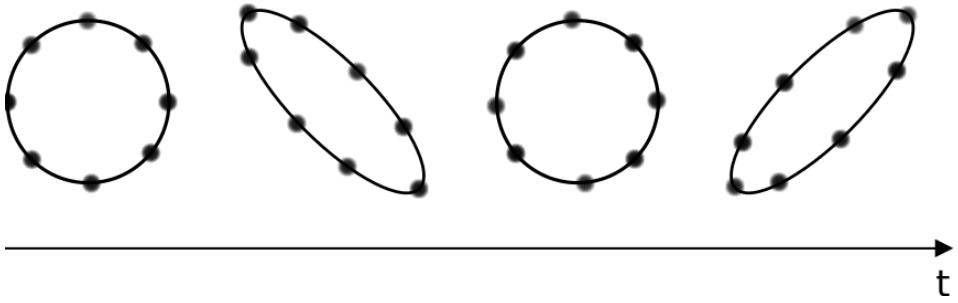

(b) × polarized wave effect

Figure 1.1. Gravitational wave effect on a particles ring

We observe in figure 1.1 what happens to a circle of particles which interact with a GW polarized + o ×[4]. We can see that in both cases the wave has an opposite action on two perpendicular axes.

What can be observed up to this point shows us why GWs are much more difficult to detect in respect of the electromagnetic waves:

- as well-known, on a macroscopic scale the gravitational field is intrinsically weaker than the electromagnetic one;
- the multipole development implies that the quadrupole potential scales with the minus third power of the source distance ($\sim r^{-3}$), while the dipole potential (needed for the electromagnetic generation) scales only with the minus second power of the source distance

The detection strategy for a GW uses the opposite action on perpendicular axes, using a Michelson interferometer (figure 1.2) to measure the length difference of the two arms introduced by GW action. The Virgo and LIGO detectors are based on this schema.

The first indirect evidence of GWs existence have been found in 1981 [30], after the discovery of the first radio-pulsar belonging to a binary system (1974 – Hulse and Taylor - PSR B1913+16 [19]). Hulse and Taylor discovered a reduction of the orbital period of the pulsar around the companion, accordingly to what provided by the General Relativity theory. In the next years, the discovery has been confirmed by further studies on the

[4]We shall note that GW action cannot be observed on a single point of the space if not related to another one.

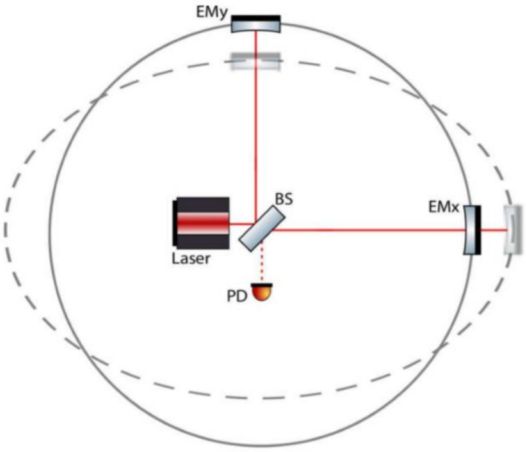

Figure 1.2. Simple schematic of Michelson Interferometer and the effect of a + polarized GW on it. The laser is split by the beamsplitter (BS). The end mirrors (EMx, EMy) reflect the laser back to the Photodiode (PD).

same binary system and others discovered afterwards. We just mention the only system known made of two pulsars, PSR J0737-3039[24].

The first direct evidence of a gravitational wave came on September 14, 2015, when for the first time GWs coming from coalescing black holes have been detected [4]. During the last four years many Compact Binary Coalescence events have been observed [17], including one produced by two Neutron Star, but other types of GW signal remain still undetected.

1.1 Type of Signals

The standard GW classification includes both transient and CW signals. In the first category we can find the already detected signals (Compact Binary Coalescences) and *Bursts*, while in the second one there are GWs emitted by compact binary objects that are very far from the coalescence (with the frequency outside the lower boundary of Earth detectors), GWs emitted by non-axisymmetric spinning neutron stars and the Stochastic Background.

Non-axisymmetric spinning neutron stars emit almost monochromatic CWs (i.e. the first time derivative of the frequency $\dot{f}$ multiplied by the observation time T_{OBS} is much smaller than the frequency of the wave f, $\dot{f}\,T_{\mathrm{OBS}} << f$) [29]. Being long-term signals, the power amplitude is very small and thus it is possible to search only for galactic sources. There are many known sources of this kind, such as Crab and Vela, as well as several other unknown sources (the estimated sources are $\sim 10^8$, while the known ones are $\sim 10^3$ [27]). Although they have a low amplitude, their persistence allows us to integrate the received power over time, studying their evolution. Furthermore, being continuous, once we have a detection, we can look back at the past data for hints on the presence of the source, and use this information as confirmation of the detection.

Stochastic GWs Background contains the residual gravitational emission of the first

moments after the Big Bang and the overlap of CWs that are too far and/or too weak to be detected separately[29].

Burst They are very short (even less than 1 millisecond) events produced by supernovae explosions or *Gamma Ray Bursts*. Being transient signals, but extremely energetic phenomena, they are associated to a strong GW emission[29].

Binary system Coalescence is one of the main GW sources. It refers to very compact objects, such as Neutron Stars and/or Black Holes. These processes are composed by 3 distinct phases: *inspiral*, *merger* and *ringdown*. During the inspiral phase the two objects emit almost CWs, with frequencies that are multiple of their inverse period. These frequencies are too low to be detected by Earth detectors (such as LIGO and Virgo) that have a minimum detectable frequency equal to 10Hz, but they might be detected using Space-based detectors (such as eLISA [13]). When the binary system is close to collapsing, we have the second and the third phases. The continuous signal becomes transient going through a fast *merger* phase where the two bodies get closer. The emitted signal is a chirp that reaches high frequencies and is detectable by Earth detectors. In the *ringdown* phase the two bodies become a new stable object with a mass that is lower than the sum of the starting body masses as the rest has been emitted in form of GWs[29].

In this discussion, we will focus on CWs emitted by neutron stars, which are crucial both to improve our knowledge about these fascinating source population, and to better understand their equation of state. This kind of source is also likely to be detected in upcoming advanced LIGO/Virgo runs. As we will see further, the expected signal is quasi-monochromatic with a very small time derivative of the frequency ($O(10^{-10}$Hz/s)), which is referred to as *spindown*. We consider a spinning neutron star with a small axymmetry -such as small mountain on the star (O(1 cm), [18]). In this case, the frequency of the wave is expected to be twice the spinning frequency, the spindown depends on the ellipticity of the star, and the expected polarization depends on the angle between the spin axis and the line of view.

We note that the antenna pattern (i.e.: the response of the antenna to the signal polarization, [9, 23]) depends on the direction of incidence of the wave (or equivalently the position angles in the sky plane), and the frequency needs to be corrected for the Doppler effect due to the Earth motions. Thus the signal is described by 8 source parameters (amplitude, starting phase of the signal, 2 polarization parameters, frequency, spindown, 2 sky coordinates) and, based on the number of known parameters, we can perform different searches.

Targeted Search Using the astrophysical knowledge of the pulsar population and using a specific emission model (e.g.: the one described above) we can find a very precise wave form and look for it through a matched filter technique which is computationally very cheap, and it is possible to run on a laptop. This type of search may or may not include the polarization parameters, having a 2- or 4-dimension parameter space. The targeted search used by the Rome Virgo group is the *5-Vector search* [9] and will be discussed further.

Narrow Band Search Considering a given uncertainty on the frequency and spindown parameters, it is possible to perform a search that is broader than a targeted one, searching for 6 parameters, including very narrow ranges for frequency and spindown. The narrow band search is coherent [26] and can be performed on a laptop.

Directed Search If we have no information on frequency and spindown, we need to perform a directed search, where the only known parameter is the position in the sky. The computational cost associated to such search is so high that requires the usage of server farms.

All-sky search This search assumes no information on the source and, since it must cover 8 parameters, it is unlikely to perform a coherent search even when using a server farm. Because of that, we need to use hierarchical approaches such as the Frequency-Hough [12] algorithm, which is extensively used and generalized in the current thesis.

In this Ph.D. thesis, we have optimized the all-sky *FrequencyHough* pipeline, using the search for a given pattern into a given data set as a trigger for the presence of CWs [Chapter 2]. We have also studied how to improve the targeted search pipeline *5vector* to include alternative polarizations to those that are assumed by GR [Chapter 3].

All those studies have been done with the first and second datasets from advanced LIGO detectors (Livingston and Hanford, [1]).

Chapter 2

Doppler Correlation Vetoes

In this chapter we will present the main part of the work, which is a new chain of vetoes apt to improve CW all-sky searches using the Doppler-based parameter-space correlations present in the data. This work has been recently published in [21].

2.1 Background

In this section we will present the *FrequencyHough* all-sky pipeline[12], where the new solution has been studied.

2.1.1 Signal Model

The expected CW signal is quasi-monochromatic, with a strain amplitude that can be written (in the detector frame) as [10]

$$h(t) = H_0(H_+ A_+ + H_\times A_\times)e^{j(\omega(t)t+\Phi_0)}, \tag{2.1}$$

where H_0 is the overall signal amplitude, H_p with $p \in (+,\times)$ is the complex component of the corresponding $(+,\times)$ polarization, A_p is the antenna response for a given polarization, ω is 2π times the signal frequency $f(t)$ and Φ_0 is the phase at a particular reference time.

There are various mechanisms by which a Neutron Star can emit CWs, but we are considering the case where $f(t) = 2f_{\text{rot}}$, where f_{rot} is the rotational frequency of the star that rotates around one of its principal axes of inertia.

If we consider a generic elliptic polarization for the incoming signal, H_p can be written as

$$H_+ = \frac{\cos 2\psi - j\eta \sin 2\psi}{\sqrt{1+\eta^2}}, \qquad H_\times = \frac{\sin 2\psi + j\eta \cos 2\psi}{\sqrt{1+\eta^2}}, \tag{2.2}$$

where η is the ratio between the semi-minor and semi-major axis of the ellipse (positively signed for counter-clockwise polarization and negatively for clockwise polarization), while ψ is the polarization angle between the celestial parallel of the source and the major axis.

The antenna response A_p can be written also as [10]

$$A_+ = a_0 + a_{1c}\cos\Omega t + a_{1s}\sin\Omega t + a_{2c}\cos 2\Omega t + a_{2s}\sin 2\Omega t, \tag{2.3a}$$
$$A_\times = b_{1c}\cos\Omega t + b_{1s}\sin\Omega t + b_{2c}\cos 2\Omega t + b_{2s}\sin 2\Omega t, \tag{2.3b}$$

where Ω is the Earth sidereal angular velocity. The a, b coefficients depend on the source and detector positions. As shown in [12, 2], the notation we use is completely equivalent to the standard one (e.g. from [23]) through the following relationships:

$$H_0 = h_0\sqrt{\frac{1+6\cos^2\iota+\cos^4\iota}{4}}, \tag{2.4}$$
$$\eta = -\frac{2\cos\iota}{1+\cos^2\iota}, \tag{2.5}$$

where ι is the angle between the star rotation axis and the line of sight, while h_0 is the ordinary GW strain amplitude.

The signal frequency is a non-trivial function of time: the frequency itself changes because of the loss (or gain) of the source's rotational kinetic energy and the signal received on Earth is Doppler-modulated by Earth motions.

We assume that the signals are quasi-monochromatic, and any time derivative of higher-order than first is null. The signal received at the observatory can be written as

$$f(t) = (f_0 + \dot{f}\,t)\left(1 + \frac{\vec{v}\cdot\hat{n}}{c}\right), \tag{2.6}$$

where f_0 is the frequency at $t = 0$, $\dot{f}$ is the frequency first-order time derivative (spindown), $\hat{n}$ is the versor representing the source position, c is the speed of light, and $\vec{v} = \vec{v}_{\rm rot} + \vec{v}_{\rm rev}$ is the Earth velocity, which is given by the sum of the Earth rotation around its axis and the revolution around the Sun.

2.1.2 Standard All-Sky Hough-transform technique

Data cleaning The search parameter space has eight dimensions, *i.e.* the starting frequency, spindown, source sky location (e.g. ecliptic coordinates λ and β), polarization constants η and ψ, starting phase Φ_0 and signal strain amplitude H_0. However, the hierarchical search we consider allows us to reduce such number to five, losing information on the polarization and the starting phase, and lowering the precision on the other parameters [12].

The analysis begins with the detector time series data. This dataset is cleaned, removing any known disturbances, as the time glitches or spectral lines (e.g. the mirrors vibration mode). Without this removal, the sensitivity of the search would be significantly reduced. This removal is divided in two steps: the noise event identification and removal[8].

The sensitivity of the detector varies in time because of the non-stationary noises. This means that, if we want to set a threshold to identify these noisy events, it should be

adaptive (i.e. changing in time). Let's call x_i our data sample: the background is valuated as the auto-regressive mean of the square modulus of x_i:

$$y_i = x_i + w y_{i-1}, \tag{2.7a}$$
$$q_i = x_i^2 + w q_{i-1}, \tag{2.7b}$$

where $y_0 = 0$, $q_0 = 0$ and

$$w = \mathrm{e}^{-\frac{\delta t}{\tau}}, \tag{2.8}$$

where δt is the sampling time and τ is a time-like memory term that have been used for the auto-regressive mean. Being w a weigh term, the mean normalization term Z_i is built from w according to $Z_i = (1 - wZ_{i-1})$, with $Z_0 = 0$. The mean and the standard deviation are then computed as

$$\mu_i = \frac{y_i}{Z_i}, \tag{2.9a}$$
$$\sigma_i = \sqrt{\frac{q_i}{Z_i} - \mu^2}. \tag{2.9b}$$

To set a threshold to identify the time glitches, we define the *Critical Ratio* (CR) detection statistic as

$$\mathrm{CR} = \frac{x_i - \mu_i}{\sigma_i}. \tag{2.10}$$

The memory term and the threshold are set depending on the detector and the dataset properties.

When the CR of an event overcomes the fixed threshold, we consider to have found an event. The event ends when it remains below the threshold for a certain time (fixed to 1 second). The data between the starting and the ending time of the event are set to 0. Also, the data in a region of 0.1 s before the beginning and after the ending of the noise are linearly set to 0.

Time-frequency study Once removed the time disturbances, the time series is divided in small chunks interlaced by half for a FFT transform. The dataset is windowed to reduce the power dispersion due to the finite length.

As is well known for a FFT, the time length of the dataset is related to the size of the frequency discretization δf. This length must be such that the frequency variation due to spindown and Doppler effect is less than one frequency bin. The result of such a transform is called SFDB (Short Fourier transform Data Base)[12, 11]. There are four sets of SFDBs with different durations, *i. e.*:

- $T_{\mathrm{FFT}} = 8192$ s for the $[10, 128]$ Hz frequency band,
- $T_{\mathrm{FFT}} = 4096$ s for the $[128, 512]$ Hz frequency band,
- $T_{\mathrm{FFT}} = 2048$ s for the $[512, 1024]$ Hz frequency band,
- $T_{\mathrm{FFT}} = 1024$ s for the $[1024, 2048]$ Hz frequency band,

where T_{FFT} is the time length of the Fast Fourier Transform (FFT).

For each of the N FFTs in the SFDB, we compute the square modulus of the FFT $S_i^P(f)$ for $i = 1, ..., N$ and the auto-regressive average spectrum $S_i^{AR}(f)$ and from those values we evaluate the ratio

$$R(i,j) = \frac{S_i^P(f)}{S_i^{AR}(f)}, \tag{2.11}$$

where i spans the time chunks and j the frequency bins. If this ratio exceeds a given threshold θ and it is also a local maxima, we call for a peak. Note that we don't keep the information on the amplitude of the peaks (differently from other all-sky pipelines), but each peak counts the same value.

This collection of peaks is called *peakmap*.

Grid definition and Doppler correction After the peakmap definition, a sky grid is defined and built using the geocentric ecliptic coordinates (λ, β). The longitude step $d\lambda$ is defined as the angular separation between two sky points, which have the same latitude β and are such that their frequency difference (due to the Earth Doppler motion) is confined within one frequency bin $df = 1/T_{\mathrm{FFT}}$ [12], *i.e.*:

$$d\lambda = \frac{c}{f\, v_{\mathrm{rev}}\, T_{\mathrm{FFT}}} \frac{1}{\cos\beta} = \frac{1}{N_D \cos\beta}, \tag{2.12}$$

where N_D represents the maximum shift due to the Doppler effect expressed as number of frequency bins[1]:

$$N_D = f\, v_{\mathrm{rev}}\, T_{\mathrm{FFT}}/c. \tag{2.13}$$

Analogously, we can identify a latitude step $d\beta$:

$$d\beta = \frac{c}{f\, v_{\mathrm{rev}}\, T_{\mathrm{FFT}}} \frac{1}{\sin\beta} = \frac{1}{N_D \sin\beta}. \tag{2.14}$$

Then, we proceed on building up the sky grid, which consists of $4\pi N_D^2$ points [12]. The peakmap is then corrected for the Doppler effect evaluated for each sky-grid point.

Hough Transform This corrected peakmap is used as input of the *FrequencyHough Transform*[12]. The Hough Transform belonging to the image recognition field is very powerful to detect linear patterns (for a summary on the Hough transform, refer to section A.2).

In this case, we transform the time-frequency plane (f, t) to the frequency-spindown plane $(f_0, \dot{f})$, according to

$$f = f_0 + \dot{f}\, t, \tag{2.15}$$

where f_0 and $\dot{f}$ are the frequency and the spindown of the source at the starting 0 time. This transform is also properly weighted for non-stationarity noise and time-varying detector response [28, 5].

[1] We note that the maximum Doppler shift is $S_D = f_0\, v_{\mathrm{rev}}/c$, while the frequency bin width is $df = 1/T_{\mathrm{FFT}}$. The ratio S_D/df is equal to N_D.

For each sky location peakmap, and for each 0.05 Hz, the two most significant local maxima candidates are selected [12].

We evaluate the significance of a candidate using the numbercount detection statistic [12]. The numbercount of a certain (m_0, q_0) point in a Hough map corresponds to how many points in the original plane (x, y) are compatible with a given straight line $y = m_0 x + q_0$, with slope m_0 and intercept q_0.

Finally, the spindown resolution $d\dot{f}$ is defined such that the maximum frequency variation for a spindown difference $d\dot{f}$ during the observing time T_{obs} is one frequency step df, *i.e.* $d\dot{f} = \frac{df}{T_{\text{obs}}}$.

In the following, we present the post-processing steps that are typically performed in an all-sky FrequencyHough search.

Clustering We cluster candidates by (a normalized) distance, which is defined as

$$d(c_1, c_2) = \sqrt{\left(\frac{\Delta f}{df}\right)^2 + \left(\frac{\Delta \dot{f}}{d\dot{f}}\right)^2 + \left(\frac{\Delta \lambda}{d\lambda}\right)^2 + \left(\frac{\Delta \beta}{d\beta}\right)^2}, \tag{2.16}$$

where "Δ" is the parameter difference and "d" is the parameter step.

The clusters are built as follows: the candidate c_j belongs to the cluster Γ_i if the distance between that and at least one candidate in the cluster is smaller than a fixed distance d_{clust} (that is a parameter of the cluster procedure), *i.e.*:

$$c_j \in \Gamma_i \quad \Leftrightarrow \quad \exists c_k \in \Gamma_i \mid d(c_j, c_k) < d_{\text{clust}}. \tag{2.17}$$

Coincidences

Given multiple datasets, we look for coincident clusters. Hence, we select clusters with at least one candidate within a distance smaller or equal to a given d_{FH} from a candidate in other cluster(s). For each set of coincident clusters, the closest couple of candidates are chosen as being coincident. The distance between these two candidates is stored as *coincidence distance*. All non-coincident candidates are then removed. Generally, d_{clust} and d_{FH} are set to 3 [12, 5, 3].

Ranking

Candidates are finally ranked as follows:

- the frequency range is split into 0.1 Hz bands;
- for each frequency band, candidates are sorted by coincidence distance in ascending order and the j-th candidate gains a rank $r_{j,\text{d}} = 1/n_j$, where n_j is the position of the candidate in the sorted list;
- for each frequency band and for each dataset, candidates are then sorted by numbercount in descending order, and they gain a new rank $r_{j,i} = 1/n_{j,i}$, where $n_{j,i}$ is the position of the j-th candidate in the sorted-list created for the i-th dataset ($i = 1, ..., N$ for N datasets).

In this way candidates gain $N+1$ ranks. An overall rank is defined as $R_j = r_{j,\mathrm{d}} \times \prod_{i=1}^{N} r_{j,i}$. Then, for each frequency band, the candidate with the highest overall rank R_j is selected to be further followed up [5].

2.2 Doppler-modulation based vetoes

In this section we describe a novel method to filter out false positive CW candidates. Based on simulations, we note that when we are in the neighborhood of CW signals (*i.e.*, when the frequency is within the maximum Earth Doppler shift from the signal frequency, which is $\sim 10^{-4}$ times the CW frequency):

- the candidate distribution is not uniform in the search parameter space, and candidates tend to lay along precise patterns;
- the numbercount along these patterns tends to be higher than in the rest of the map;
- the numbercount drops slower along these patterns than in any other direction.

Before describing the details of such patterns in section 2.2.2, we want to highlight that the number of typical candidates returned by the Hough transform (and described in section 2.1.2) is $\sim 10^{10}$ for the [20,2000] Hz frequency band and $[-10,2] \times 10^{-9}$ Hz/s spindown band. However, the bulk of them are produced by unknown detector disturbances uniformly distributed in the search parameter space, while only a small portion of them ($O(10^3)$) can be attributed to instrumental lines of known origin [14]. These behave as signals coming from the poles, and that create patterns similar to those produced by real CWs.

In the presence of real signals, which are not surrounded by loud noise artefacts, we expect candidates originated by them to have the highest numbercount values. However, rather than identifying directly the candidate that describes at best a real CW signal, we first look for the related pattern structure as it is an easier feature to be identified.

2.2.1 Pattern generation

Let us assume to observe a point in the sky-plane close enough[2] to the signal sky position. The residual Doppler effect will spread the time-frequency peaks around the right $f(t) = f_0 + \dot{f}\,t$ frequency-time line. The Hough transform will match this spread line accounting for the residual Doppler effect through a modification of the spindown. In a similar way, the maximum numbercount candidate will not have the right frequency nor spindown, but the shift will be due to the (residual) Doppler effect. As a consequence, the numbercount value associated to a given candidate will be lower than the one expected for the right parameters, and the difference will be correlated to how much the residual Doppler effect spreads the signal on the different $f(t) = f_0 + \dot{f}\,t$ lines (or equivalently how much the residual Doppler sinusoid modulated line differs from a straight line). Since the patterns are related to the (residual) Earth Doppler effect, we can simplify (2.6) performing some approximations to obtain a formula that contains the source parameters

[2] In this case "close" refers to a distance such that the residual Doppler effect shifts the frequency of the signal no more than a single frequency bin.

$(\lambda,\ \beta,\ f_0,\ \dot{f})$. As a first step, we neglect the rotation component $v_{\rm rot}$ as it is 10^{-2} times the revolution component $v_{\rm rev}$. This approximation allows us to write the scalar product as a simple function of the ecliptic coordinates (see A.1 for details):

$$f(t) = (f_0 + \dot{f}\,t)\left[1 + \frac{v_{\rm rev}}{c}\cos\beta\sin(\lambda - \Omega_{\rm rev}t)\right], \tag{2.18}$$

where $v_{\rm rev}$ is the norm of $\vec{v}_{\rm rev}$ and $\Omega_{\rm rev} = v_{\rm rev}/R_{\rm SE}$ is the Earth angular revolution velocity (considering the distance Sun-Earth $R_{\rm SE}$ to be constant). As a further approximation, we neglect the term $\dot{f}\,t\,v_{\rm rev}\cos\beta\sin(\lambda-\Omega_{\rm rev}t)/c$ as we search for $\dot{f} \in [-10,2]\times10^{-9}$ Hz/s, and consider a standard observing time $T_{\rm obs}$ (of the order of few months). Hence, we obtain $\dot{f}\,T_{\rm obs}\,v_{\rm rev}/c << 1$ Hz and

$$f(t) = f_0\left[1 + \frac{v_{\rm rev}}{c}\cos\beta\sin(\lambda - \Omega_{\rm rev}t)\right] + \dot{f}\,t. \tag{2.19}$$

It is useful to perform the time derivative of (2.19), *i.e.*:

$$\frac{d}{dt}f(t) = -f_0\frac{v_{\rm rev}\Omega_{\rm rev}}{c}\cos\beta\cos(\lambda - \Omega_{\rm rev}t) + \dot{f}, \tag{2.20}$$

remembering that $\dot{f}$ is not a function of time but a source parameter. Equations (2.19) and (2.20) will be used to identify the functional form of the patterns in the data.

2.2.2 Pattern types

To describe the various patterns produced by a CW signal, we consider a software injection, *i.e.* an artificial signal added to the whole dataset from the first Advanced LIGO Observing Run (O1) [17]. The software injection parameters are: frequency $f_0 = 124.184$ Hz (at GPS epoch 1126621183 and power spectral density of $\sim 8.4\times10^{-24}\frac{1}{\sqrt{Hz}}$); sky position $\lambda = 71.5°$ and $\beta = 53.8°$; spindown $\dot{f} = 4.06\times10^{-10}$ Hz/s. The amplitude of the injected signal is $h_0 = 5\times10^{-25}$, while the inclination angle is $\iota = 97.74°$. In the following, we plot the candidates returned by the FrequencyHough algorithm (before coincidences, ranking and clustering) in the $[-2,2]\times10^{-9}$ Hz/s spindown range for the whole sky and the [124.174, 124.194] Hz frequency interval.

The sky-plane pattern. Figure 2.1 shows the numbercount (colorbar) of candidates as a function of the sky-plane. We can observe how the numbercount drops moving away from the signal sky position. It is straightforward to see that looking for curves in the sky-plane, like that of (2.18) is constant, corresponds to the $\cos\beta\sin(\lambda-\Omega_{\rm rev}t)$ function being constant. We refer to these curves as constant Doppler-effect curves, and we use (2.18) to identify them.

Candidates shown in figure 2.1 are time independent as the FrequencyHough transform converts the frequency-time peaks into the frequency-spindown domain, and thus the frequency no longer depends on time (as described in section 2.1.2). Since the Hough transform corresponds to an integration over time, we can replace the time dependence in $\cos\beta\sin(\lambda-\Omega_{\rm rev}t)$ with a longitude-like constant Λ, obtaining

$$\rho(\lambda,\beta) = \cos\beta\sin(\lambda - \Lambda), \tag{2.21}$$

where ρ is the function describing the sky-plane patterns that are represented in figure 2.1. We note that Λ depends only on the starting and ending times of the detector observing

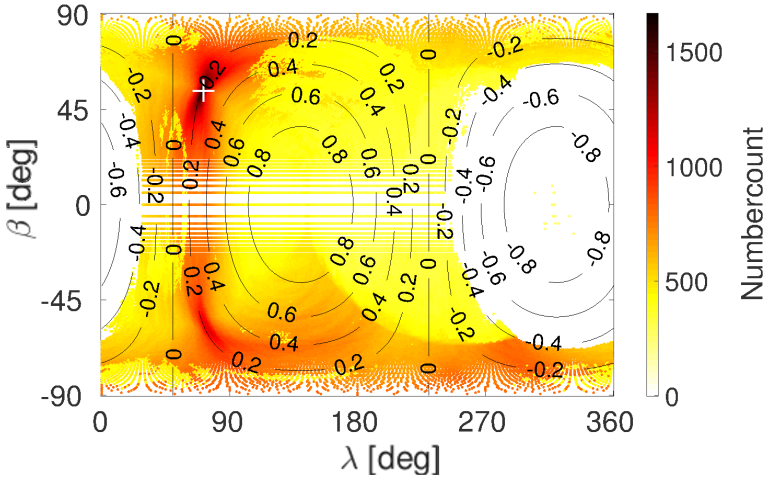

Figure 2.1. Candidates in the sky plane, such that their frequency is in the range $[f_0 - 0.01\text{ Hz}, f_0 + 0.01\text{ Hz}]$. The white cross corresponds to the source sky position, which is $\lambda = 71.5°$ and $\beta = 53.8°$. The contours correspond to the values of (2.21). The horizontal stripe pattern around $\beta = 0$ is an artifact, which is due to the discretization step during the computation of the Hough transform.

run (see A.3). In the current O1 study, $\Lambda = 51.5°$. The black lines in figure 2.1 are the constant $\rho = \cos\beta\sin(\lambda - \Lambda)$ curves, with the respective values.

The frequency-sky pattern. In the following, we describe the correlation existing between the source frequency and sky position.

If we search for a signal in the wrong sky position, it might appear shifted in frequency by an amount that is related to the residual Doppler effect (as described in section 2.2.1). Although this is observable just by looking at the planes that relate frequency with only one of the sky coordinates (e.g.: frequency-λ or frequency-β planes), the correlation is more evident when studied on the plane frequency-ρ, where ρ is the sky coordinate in (2.21).

Figure 2.2 shows candidates in the $f - \rho$ plane with a linear dependence (as expected by (2.19)). The pattern in figure 2.2 is given by

$$f = F\left(1 - \frac{v_{\text{rev}}}{c}\rho\right), \tag{2.22}$$

where f and ρ are the coordinates of each candidate, while F is a constant that acts as an intercept and is related to the source parameters. If we replace f and ρ with the respective source values, we obtain a value of F_{sour} that defines the pattern that passes through the source parameter position, and has the largest numbercount candidates.

We note that the sign of (2.22) is opposite to the one in (2.19), as we are correcting for the (residual) Doppler effect by Taylor expanding in $\epsilon = v_{\text{rev}}/c$ for small ϵ, *i.e.* $1/(1+\epsilon) = 1 - \epsilon + O(\epsilon^2)$. The spindown is not present in this formula since we are considering a projection on the $f - \rho$, neglecting the spindown effect. We perform a further approximation as we note that F in (2.22) is an unknown parameter containing relevant information on the signal itself, while f and ρ are candidates coordinates. Therefore we can obtain a specific F inverting (2.22):

$$F = f \Big/ \left(1 - \frac{v_{\text{rev}}}{c}\rho\right) = f\left[1 + O\left(\frac{v_{\text{rev}}}{c}\right)\right]. \tag{2.23}$$

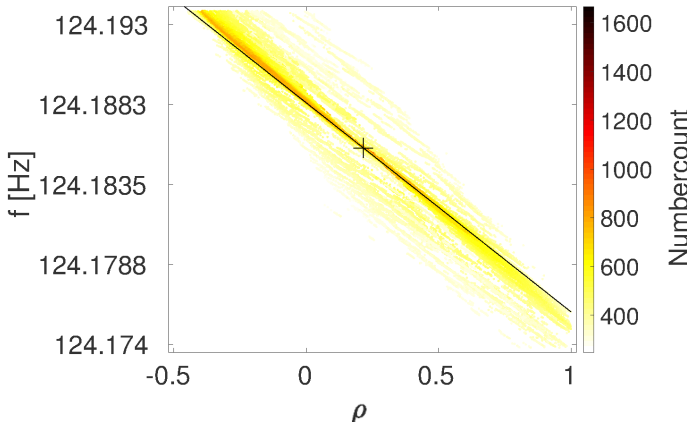

Figure 2.2. Candidates in the frequency-sky plane, such that their frequency is in the range $[f_0 - 0.01\text{ Hz}, f_0 + 0.01\text{ Hz}]$. The black cross corresponds to the source sky position, which is $\rho = 0.202$. The black line represents (2.22).

The term $O\left(\frac{v_{\text{rev}}}{c}\right)$ is not negligible as it has the same order of magnitude of the pattern size[3] (which is $2v_{\text{rev}}/c$). If we replace (2.23) into (2.22), we obtain:

$$f = F\left(1 - \frac{v_{\text{rev}}}{c}\rho\right) = F - F\frac{v_{\text{rev}}}{c}\rho = F - f\rho\frac{v_{\text{rev}}}{c} - O\left(f\rho\left(\frac{v_{\text{rev}}}{c}\right)^2\right) \tag{2.24}$$

$$\sim F - f\rho\frac{v_{\text{rev}}}{c} = F - \tilde{\rho}\frac{v_{\text{rev}}}{c}, \tag{2.25}$$

which is a linear relation between f and $\tilde{\rho} = f\rho$. Hence, we can easily find F as the intercept of a linear fit, and use v_{rev}/c as slope. If we perform a fit and find a slope that differs from the expected value v_{rev}/c, we can exclude the presence of a CW signal.

The spindown-sky pattern. We show here the correlation between the source spindown and sky position.

Since the ρ dependence on the spindown is not linear, we need to find a new sky coordinate that is linearly related to the spindown. To this purpose, we can use (2.20) in the same way as done for (2.19) (for the frequency-sky pattern). As ρ linearizes the frequency-sky correlation, we introduce a new variable that linearizes the spindown-sky relation, *i.e.*:

$$\rho' = \cos\beta\cos(\lambda - \Lambda). \tag{2.26}$$

By replacing $\Lambda \to \Omega_{\text{rev}}t$ in (2.20), we obtain the correlation represented in figure 2.3, *i.e.*:

$$\dot{f} = \dot{F} + \frac{\Omega_{\text{rev}}v_{\text{rev}}}{c}f\rho', \tag{2.27}$$

where we performed the same approximation used for (2.24), but substituting F with f, and $\dot{F}$ (which is the time derivative of F) playing the same role as F in (2.22) and (2.24).

2.2.3 Novel chain of vetoes

Based on the patterns above, we propose a new chain of vetoes to remove candidates that do not present the features described by the three correlations above. We apply these

[3] It corresponds to the frequency range where the pattern lays while changing $-1 \le \rho \le 1$.

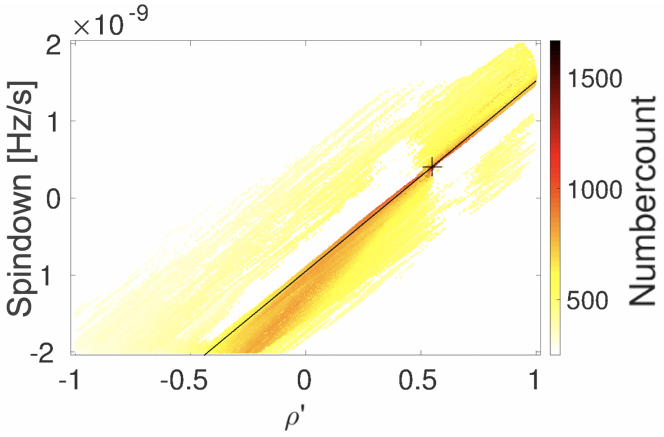

Figure 2.3. Candidates in the spindown-sky plane, such that their frequency is in the range $[f_0 - 0.01\text{ Hz}, f_0 + 0.01\text{ Hz}]$. The black cross corresponds to the source sky position, which is $\rho' = 0.555$. The black line represents (2.27).

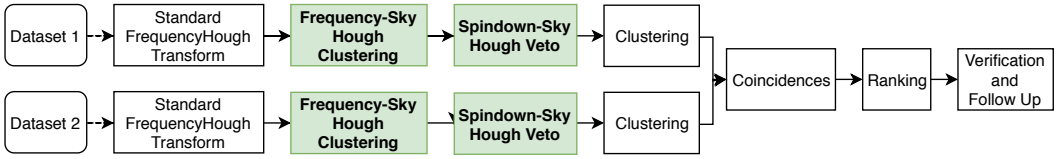

Figure 2.4. All-sky search flowchart for a two-detector analysis. The novel vetoes (shaded boxes) are added to the standard pipeline.

vetoes to all candidates returned by the FrequencyHough [12] before any post-processing (clustering, coincidences and ranking steps). In figure 2.4 we present a comparison between the standard pipeline [3] and the proposed one. The new procedure consists of two steps to be applied before the standard clustering described in section 2.1.2. In the first step, candidates are clustered according to the pattern given by (2.24), while in the second step we select the subset of candidates lying on the pattern described by (2.27).

Since the frequency-sky and spindown-sky patterns are linear, we can apply the Hough transform again in these planes to further eliminate candidates. We prefer performing a Hough transform rather than directly looking for a given linear pattern (with known slope) as the Hough transform is a more robust step, which removes some random patterns that would not be completely removed otherwise.

In the following, we show the implementation details. We refer to the standard FrequencyHough as 0-Hough, while the new Frequency-Sky Hough and Spindown-Sky Hough transforms will be referred to as 1-Hough and the 2-Hough, respectively.

Frequency-Sky Hough clustering

The first step is to look at the data for candidates lying on the pattern described by (2.24). If we are in presence of a CW signal, we would expect to find an excess of candidates (with respect to a uniform distribution) with high numbercount in the neighborhood (*i.e.*, within the maximum Earth Doppler shift) of this pattern. We know that candidates tend to gather along curves described by (2.22) (or, equivalently (2.24)) and (2.27) and that the closer we are to the pattern, the higher the numbercount of the candidates will

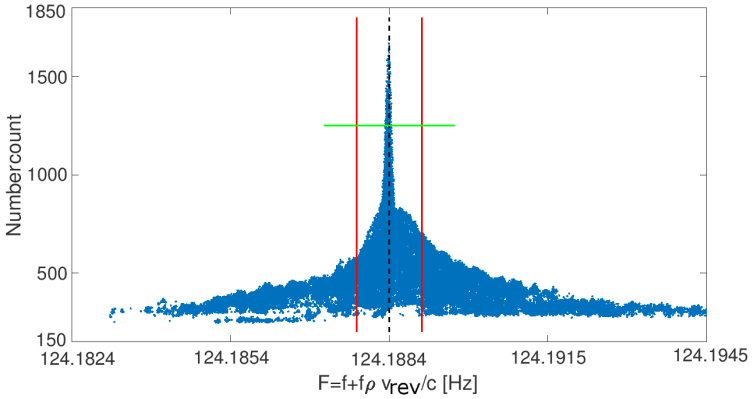

Figure 2.5. Candidate numbercount as a function of F. The dashed black line denotes the maximum numbercount values, while the solid red lines are the conservative boundaries of the δF region; the horizontal green line represent the 75% of the maximum numbercount. The injection parameters used here are those introduced in Sec. 2.2.2.

be. We use the Hough transform algorithm to find patterns described by (2.24), having an excess of high numbercount candidates. To this purpose, we Hough-transform f and $\tilde{\rho} = f\rho$ coordinates into new m and F values, and we refer to it as 1-Hough transform. Furthermore, we weight the 1-Hough transform with the numbercount of each candidate. Thus, the 1-Hough transform maps the initial candidates from the $(f, \tilde{\rho})$ plane to a new (m, F) plane according to

$$f = m\tilde{\rho} + F, \tag{2.28}$$

where F is the same of (2.24), while m is a crosscheck parameter that must correspond to $(-v_{\rm rev}/c)$ within a certain error (which has been empirically set to $0.075\, v_{\rm rev}/c$). In figure 2.5 we plot the numbercount versus F, and we note that the pattern described by (2.24) is bounded by a region of $\delta F = 10^{-5} f_0$, with f_0 being the signal frequency. This means that candidates with at least 75% of the maximum numbercount are confined in a δF region around the maximum value in the $(f + \tilde{\rho}\ v_{\rm rev}/c)$ dimension. For this reason, the F step in the new Hough grid should be equal to δF, but to avoid border effects, a refinement of 10^{-1} has been chosen, making the grid step $dF = 0.1\,\delta F$. Thus, each candidate is projected into a band consisting of 10 frequency bins with width dF each[4]. The F values are such that $F \in [f_{\rm min} - dF, f_{\rm max} + dF]$, where $f_{\rm min}$ and $f_{\rm max}$ are the minimum and maximum value of the analyzed frequency interval (*i.e.*, 1 Hz wide in our case). The dm step and m region have been found empirically, balancing performance and accuracy: $dm = 0.5 \times 10^{-5}$, while the intervals of the m axis are 1.5×10^{-4} around the value of $(-v_{\rm rev}/c) \sim -10^{-4}$, according to (2.24).

Once obtained the 1-Hough map with its relative 1-numbercount values, for each value of F, the m value that corresponds to the maximum 1-numbercount is selected. If this is consistent with $-v_{\rm rev}/c$, within a certain precision, that is empirically set to $(-1 \pm 0.075) \times 10^{-4}$, then a pattern is considered found and a cluster is created.

The rule for cluster creation is the following: we assume to find a pattern corresponding to the i-th value of F (*i.e.*, F_i) and the slope corresponding to the maximum 1-numbercount to be m_i. Then, the cluster C_i will contain all candidates $c_j = (f_j, \tilde{\rho}_j, ...)$

[4]Hence, we will have a point that will be transformed into a band, which has a size of 10 bins in frequency.

such that

$$\left| f_j - m_i \tilde{\rho}_j \right| \leq F_i (1 + \delta_{\mathrm{cl},1}), \tag{2.29}$$

where $\delta_{\mathrm{cl},1} = 2 \times 10^{-5}$ is half of the size of the cluster (the subscript 1 denotes that we are applying the first step of the veto procedure). Equation (2.29) clearly describes a band confined by the two lines $f_j = m_i \tilde{\rho}_j + F_i (1 \pm \delta_{\mathrm{cl},1})$. This process is repeated for the whole search frequency band, in steps of 1 Hz, and reduces the number of candidates caused by noise by 25%.

Spindown-Sky Hough veto

Once the clusters have been created, for each cluster, we check whether the second pattern described by (2.27) is present. We remind that both patterns must be present to have a loud enough signal to be detected. Thus, according to (2.27), we use a new coordinate $\tilde{\rho}' = \Omega_{\mathrm{REV}} f \rho'$ (with ρ' that is defined in (2.26)) to perform a new Hough transform for the linear pattern (equivalent to (2.27)):

$$\dot{f} = m \tilde{\rho}' + \dot{F}, \tag{2.30}$$

where $\dot{F}$ is the same as (2.27), and m represents a crosscheck parameter that must be, this time, $\sim v_{\mathrm{rev}}/c$. Thus, for each cluster obtained in the previous step, a Hough map is computed. The size of the m space has been empirically set (with the same criterion as for the 1-Hough step) between 0.5×10^{-4} and 1.5×10^{-4}. The step dm is the same as in section 2.2.3.$\dot{F}$ has been chosen according to (2.30) within the time derivatives

$$\dot{F}_{\mathrm{min}} = \dot{f}_{\mathrm{min}} - 2 f_{\mathrm{clust}} \Omega_{\mathrm{rev}} v_{\mathrm{rev}} / c, \tag{2.31}$$

and

$$\dot{F}_{\mathrm{max}} = \dot{f}_{\mathrm{max}} + 2 f_{\mathrm{clust}} \Omega_{\mathrm{rev}} v_{\mathrm{rev}} / c, \tag{2.32}$$

where f_{clust} is the mean frequency in the chosen cluster.

From the Hough map in the $(m, \dot{F})$ plane, the maximum numbercount (M) is found as well as the corresponding $(m_{\mathrm{M}}, \dot{F}_{\mathrm{M}})$. If $m_{\mathrm{M}} = v_{\mathrm{rev}}/c$ (as expected), within a relative empirical error of 7.5%, a particular cluster is kept for further vetoes, otherwise it is rejected. If the cluster is kept, we select only candidates such that

$$\left| \dot{f} - m \tilde{\rho}' \right| \leq \dot{F} + \delta_{\mathrm{cl},2}, \tag{2.33}$$

where $\delta_{\mathrm{cl},2} = 10\, d\dot{f}$ is half of the size of the cluster (the subscript 2 denotes the second veto). This step further reduces all candidates (remaining from the first veto) by $\sim 30\%$. The candidates that survive to this veto procedure are processed by the standard pipeline (as shown in figure 2.4), performing clustering, coincidences and ranking (see section 2.1.2).

2.3 Comparison to the standard FrequencyHough algorithm

The new veto chain drastically reduces the false alarm probability allowing us to select significant candidates with more robust criteria. To make a clear assessment, we used

a set of 501 software injections[5] running the standard 0-Hough transform, and then applied the new chain of vetoes and checked how many signals were potentially lost with respect to those recovered by the standard pipeline. For each Hz in the interval [11, 128] Hz, a fake signal has been injected in both Hanford and Livingston O1 datasets, with frequency randomly chosen in each Hz, and spindown in $[-10, 2] \times 10^{-9}$ Hz/s, with uniform distribution across all sky, and amplitude values of h_0 equal to 10^{-24}, 2.2×10^{-25} and 1.4×10^{-25} (for a total of 351 software injections). For each of these three h_0-amplitudes, we repeat this procedure again 10 times per Hz, drawing every time a uniform distribution over the sky and in the spindown range of $[-10, 2] \times 10^{-9}$ Hz/s, and for each Hz in the interval [120, 125] Hz region to investigate deeper in such region (for a total of 150 software injections). For the highest amplitude value ($h_0 = 10^{-24}$), 100% of the candidates (produced by an injection) present after the 0-Hough are still present after the novel chain of vetoes (*i.e.* after applying the 1-Hough and 2-Hough steps). For the middle amplitude value ($h_0 = 2.2 \times 10^{-25}$), 2% of the injected signals are lost in the Livingston detector, while no candidates (caused by an injection) are lost for the Hanford detector. In this case, by visual inspection, we verified that the lost candidates (caused by injections) were close to unknown instrumental disturbances [14]. For the lowest amplitude value ($h_0 = 1.4 \times 10^{-25}$), the loss is equal to 7% and 14% for the Hanford and Livingston datasets, respectively. In this case the lost candidates (caused by injections) were at frequencies below 80 Hz, where the injected signal amplitude is smaller than the estimated sensitivity[6] [5].

For each set of injections, after the coincidence steps, we have 0%, 2% and 23% of losses, respectively. The 1-Hough clustering step reduces the number of candidates by $\sim 30\%$, while the 2-Hough veto by $\sim 40\%$. This results into an overall reduction of $\sim 60\%$ for the whole veto chain.

Further tests have been done using data from the second Advanced LIGO-Virgo observing run (O2) [17]. We used O2 data to perform an all-sky search for the [10, 2048] Hz frequency band and the $[-10, 2] \times 10^{-9}$ Hz/s spindown band. We compared the results obtained adding the two new vetoes described here with those obtained by the standard FrequencyHough, which are reported in [3]. We found that the 1-Hough veto (presented in section 2.2.3) removes $\sim 30\%$ of candidates in the frequency band [10, 128] Hz, $\sim 25\%$ in [126, 1024] Hz, and $\sim 20\%$ in the [1020, 2048] Hz frequency band. The 2-Hough veto (presented in section 2.2.3) removes 60% of candidates in the [10, 128] Hz, and $\sim 40\%$ in the remaining frequency regions. Thus, the overall veto chain removes $\sim 70\%$ in the frequency band [10, 128] Hz, $\sim 55\%$ in the frequency band [128, 1024] Hz, and $\sim 50\%$ in the frequency band [1024, 2048] Hz. These results are summarized in Table 2.1.

Software-injection tests have been done also in O2 data. We used a set of 436 software injections, which are distributed as follows. For each Hz in the interval [19, 128] Hz, two fake signals have been injected in both Hanford and Livingston O2 datasets, with frequency randomly chosen in each Hz from the above range, and spindown in $[-2, 10] \times 10^{-9}$ Hz/s, with uniform distribution across all sky, and amplitude values of h_0 equal

[5] For all software injections presented here we have assumed $-\pi/2 \leq \psi \leq \pi/2$ and $-1 \leq \eta \leq 1$ to be uniformly distributed.

[6] We note that there are two cases where the new vetoes stop working efficiently, *i.e.* for signal-to-noise ratios ≤ 1 (the searched patterns are no longer identifiable) and/or when the frequency of a noise disturbance falls into a 10^{-4} Hz region centered around the signal (injection) frequency, and has a numbercount which is larger than the one caused by the injection.

analyzed frequency band	1-Hough	2-Hough	Overall
[10, 128] Hz	30%	60%	70%
[126, 1024] Hz	25%	40%	55%
[1020, 2048] Hz	20%	40%	50%

Table 2.1. Removal of candidates after applying the 1- and 2-Hough transform based vetoes as compared with the standard FrequencyHough using the O2 data set. See main text for details.

h_0	Before coincidences	After ranking		Candidates	
$[10^{-25}]$	Loss	Gain	Loss	Before Coincidences	After Ranking
5.5	H ~ 3.8% L ~ 0.5%	4%	5%	~ 40%	~ 50%
2.2	H ~ 8.6% L ~ 3.8%	14%	11%		

Table 2.2. Comparison between the new sets of vetoes included in the standard algorithm and the standard FrequencyHough algorithm itself for the fake signals added to the O2 dataset, for Hanford (H) and Livingston (L) detectors, respectively. The “Gain" (“Loss") refers to the candidates caused by the injections recovered (lost) when including the new sets of vetoes, but lost (recovered) by the standard FrequencyHough algorithm. The column “Candidates" denotes the percentage of candidates that we find when considering the new set of vetoes with respect to those we find with the FrequencyHough algorithm.

to 5.5×10^{-25} and 2.2×10^{-25} (for a total of 436 = 2 injections ×109 Hz ×2 different amplitudes).

For the highest amplitude value ($h_0 = 5.5 \times 10^{-25}$), 3.8% and 0.5% of the injected signals are lost for the Hanford and Livingston datasets, respectively, after applying the 1-Hough and 2-Hough steps. For the lowest amplitude value ($h_0 = 2.2 \times 10^{-25}$), the loss is equal to 8.6% and 3.8% for the Hanford and Livingston datasets, respectively. In this case, the lost candidates (caused by injections) were at frequencies below 80 Hz, where the injected signal amplitude is smaller than, or comparable with, the estimated sensitivity [3]. For each set of injections, we performed the clustering, coincidence and ranking step without applying the chain of vetoes (as in the standard pipeline) and applying the chain of vetoes. The results are the following: the number of candidates has been reduced by 50% with the new pipeline (with respect to the standard one). Some of the injections retrieved by the standard pipeline are not recovered by applying the new vetoes (about 5% for the highest amplitude and 11% for the lowest amplitude), but the new pipeline has recovered some of the injections that were lost in the standard pipeline (about 4% and 14% for the highest and lowest amplitude values, respectively). On the other hand, the removal procedure allowed other candidates (caused by injections) to stand from the ranking step and pass to the next stage. This corresponds to a same rate of recovery, with the false alarm rate reduced by the 50%. Results are summarized in Table 2.2.

As a further clarification , in figure 2.6 we show a graphical example of the candidates produced by the FrequencyHough when a software injection is added to the analyzed data set and the new chain of vetoes is applied.

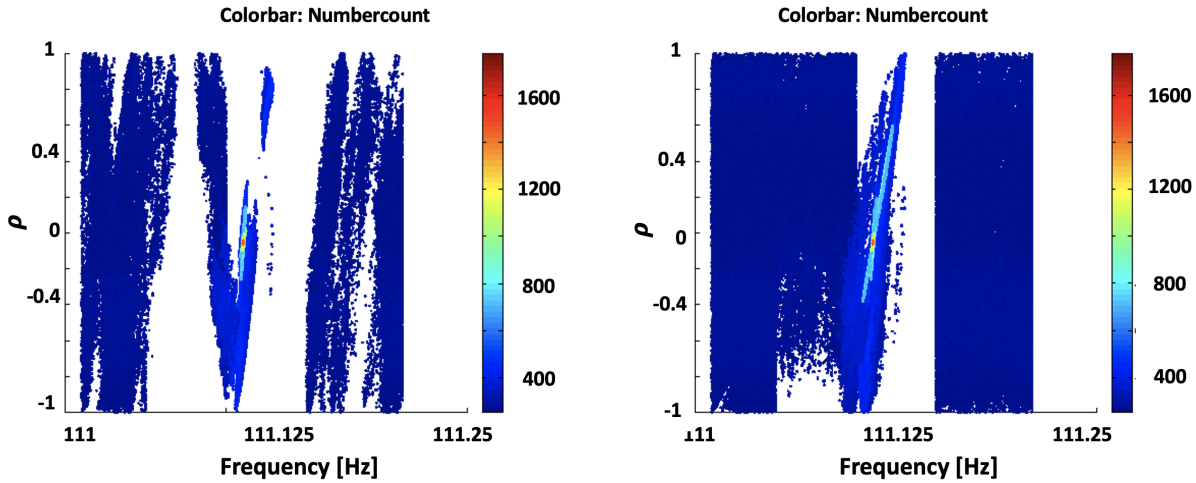

Figure 2.6. Candidates obtained by the FrequencyHough after (left panel) and before (right panel) the veto chain, when a software injection is added at 111.11 Hz (with a spindown value of 1.28×10^{-9} and a signal-to-noise ratio of 6). Due to the Doppler effect, the software injection generates candidates that cover a ~ 0.022 Hz region.

2.4 Conclusions

The chain of vetoes proposed in this chapter is an effective improvement to the FrequencyHough pipeline. This is used to search for CW signals as it brings a reduction of more than half of the false-positive candidates, allowing us to follow up only the most significant candidates. This relevant reduction gives us also the chance to improve the depth of the search including candidates that would be otherwise excluded due to computational constraints. We plan to use the new vetoes to perform a real all-sky search for CWs using data collected from the ongoing third Advanced LIGO-Virgo detector run.

The computing cost budget is assessed in A.4.

Chapter 3

Non-GR targeted Search

In this chapter we will introduce a search for alternative polarizations with respect to those foreseen by the GR theory, and that are still present in the extended relativity theory (Non-GR). We will begin describing the actual GR pipeline for targeted searches (whose polarizations are described the first time by [16]), then we will describe the non-GR polarizations [15] and the detector response to them. Finally, we will present the ability of the GR pipeline to detect non-GR signals and a new proposal to introduce a non-GR directed search extending the actual search.

3.1 5vector method GR targeted search

We resume now the *5vector* method [9] for GR targeted searches where the signal's polarization is unknown. Although this search has two different applications, whether we know or not the signal polarization, we want to extend the method for a generic non-GR theory, thus we do not have a specific emission mechanism ([6]). In this case, we want to represent a signal with its polarization ellipse as follows:

$$h(t) = h_0(H_+\mathbf{e}_+ + H_\times\mathbf{e}_\times)\mathrm{e}^{j(\omega(t)t+\Phi_0)}, \tag{3.1}$$

where h_0 is the overall amplitude; $\mathbf{e}_p$ with $p \in \{+,\times\}$ is the tensorial basis of the GR wave; H_p is the complex coefficient of the polarization as described in section A.5. The 2 complex values can be expressed as

$$H_+ = \frac{\cos(2\psi) - \jmath\eta\sin(2\psi)}{\sqrt{1+\eta^2}}, \tag{3.2a}$$

$$H_\times = \frac{\sin(2\psi) + \jmath\eta\cos(2\psi)}{\sqrt{1+\eta^2}}, \tag{3.2b}$$

where ψ is the angle defining the direction of the major axis with respect to the celestial parallel of the source and η is the ratio between the minor and the major semi-axis, signed as negative for counterclockwise rotation on the ellipse. In that way it is easy to see that the $\vec{H} = (H_+\ H_\times)$ is normalized to 1, that means h_0 the absolute amplitude of the wave.

Using this model, the detector response is encoded into the basis. To obtain the antenna pattern we have to perform the following operation

$$h_{\text{det}}(t) = < x|h(t)|x > - < y|h(t)|y >, \tag{3.3}$$

where x and y represent the two arms vectors in the detector frame with the measurement unit equal to the arm length (i.e.: $< x| = (1\ 0\ 0)$ and $< y| = (0\ 1\ 0)$), while we have $h(t)$ (from (3.1)) in the source frame. To change the frame, we have to perform 3 rotations[23]: one to change the frame from the source to the north pole frame, one time dependent to make the frame co-moving with the Earth rotation, and one to change the framework to the detector one. These 3 rotations split the signal frequency f_0 to 5 ones, that is $f_0 + k f_{\text{rot}}$ with $k \in [-2, 2]$ and f_{rot} is the rotation frequency of the Earth.

The result can be summarized as follows:

$$h(t) = h_0(H_+ A_+ + H_\times A_\times)\mathrm{e}^{j(\omega(t)t+\Phi_0)}, \tag{3.4}$$

where $A_p = \sum_{k=-2}^{2} A_k^p$. The A_k^ps are computed as follows,

$$A_{-2}^p = \frac{1}{2}(a_{2c}^p + a_{2s}^p)\mathrm{e}^{J2\Omega_{\text{REV}}t}, \tag{3.5a}$$

$$A_{-1}^p = \frac{1}{2}(a_{1c}^p + a_{1s}^p)\mathrm{e}^{J\Omega_{\text{REV}}t}, \tag{3.5b}$$

$$A_0^p = a_0^p, \tag{3.5c}$$

$$A_{-1}^p = \frac{1}{2}(a_{1c}^p - a_{1s}^p)\mathrm{e}^{-J\Omega_{\text{REV}}t}, \tag{3.5d}$$

$$A_{-2}^p = \frac{1}{2}(a_{2c}^p - a_{2s}^p)\mathrm{e}^{-J2\Omega_{\text{REV}}t}, \tag{3.5e}$$

where the a^p are the results of the rotation calculation for each polarization (the results are presented in [9] and in section 2.1.1, but we changed the b coefficient to $a^\times$ for sake of simplicity in the next steps). The a coefficients are the following, for the + polarization

$$a_0^+ = -\frac{3}{16}\cos(2a)(1+\cos(2\delta))(1+\cos(2\lambda)), \tag{3.6a}$$

$$a_{1c}^+ = -\frac{1}{4}\cos(2a)\sin(2\delta)\sin(2\lambda), \tag{3.6b}$$

$$a_{1s}^+ = -\frac{1}{2}\sin(2a)\cos(\lambda)\sin(2\delta), \tag{3.6c}$$

$$a_{2c}^+ = -\frac{1}{16}\cos(2a)(3-\cos(2\delta))(3-\cos(2\lambda)), \tag{3.6d}$$

$$a_{2s}^+ = -\frac{1}{4}\sin(2a)(3-\cos(2\delta))\sin(\lambda), \tag{3.6e}$$

and for the × polarization

$$a_0^{\times} = 0, \tag{3.7a}$$
$$a_{1c}^{\times} = -\sin(2a)\cos(\delta)\cos(\lambda), \tag{3.7b}$$
$$a_{1s}^{\times} = \frac{1}{2}\cos(2a)\cos(\delta)\sin(2\lambda), \tag{3.7c}$$
$$a_{2c}^{\times} = -\sin(2a)\sin(\delta)\sin(\lambda), \tag{3.7d}$$
$$a_{2s}^{\times} = \frac{1}{4}\cos(2a)(3-\cos(2\lambda))\sin(\delta), \tag{3.7e}$$

where δ is the source declination, λ and a are respectively the the detector latitude and azimuth.

Using this as starting point, the detection procedure is to calculate the *data 5-vect* as

$$\mathbb{X} = \int_T x(t)\mathbb{W}\mathrm{e}^{-J\omega_0 t}dt. \tag{3.8}$$

where $\mathbb{W}$ is a 5 component vector that is $W_k = \mathrm{e}^{-Jk\Omega_{\mathrm{REV}}t}$ and $k \in [-2,2]$. Since we do not have a specific polarization-parameter-set, we can estimate the 2 observables (h_p) as follows:

$$\hat{h_+} = \frac{\mathbb{X}\cdot\mathbb{A}^+}{|\mathbb{A}^+|^2}, \tag{3.9a}$$
$$\hat{h_\times} = \frac{\mathbb{X}\cdot\mathbb{A}^\times}{|\mathbb{A}^\times|^2}. \tag{3.9b}$$

Find more details of such pipeline in [9] and relative observing papers.

3.2 Non-GR Polarization

The second step to study the non-GR polarizations is to define the additional polarization, beside + and ×. We do not want to rely on a specific non-GR theory, since we are trying to collect data beside the theory. The only assumption that we want to make in this case is that we are working in a metric theory, thus the metric tensor (and the relative wave tensor) must be symmetric: this bring us from the 16 starting elements to 10 elements of a symmetric matrix.

Furthermore, we still have 4 degrees of freedom to fix for our theory; the 4 space-time coordinates. Using this components, we can reduce to null the 4 time values in the wave tensor. In this way, our wave tensor contains only the 6 components of the symmetric space 3x3 tensor. These are the 6 polarizations expected by any metric GWs theory, where 2 are those from the GR one.

The most used non-GR polarizations in the current theoretical and data analysis studies (as in [22, 6]) are called x, y, breathing (b) and longitudinal (l). These polarizations

are the following:

$$\mathbf{e}_x = \begin{pmatrix} 0 & 0 & 1 \\ 0 & 0 & 0 \\ 1 & 0 & 0 \end{pmatrix}, \tag{3.10a}$$

$$\mathbf{e}_y = \begin{pmatrix} 0 & 0 & 0 \\ 0 & 0 & 1 \\ 0 & 1 & 0 \end{pmatrix}, \tag{3.10b}$$

$$\mathbf{e}_b = \begin{pmatrix} 1 & 0 & 0 \\ 0 & 1 & 0 \\ 0 & 0 & 0 \end{pmatrix}, \tag{3.10c}$$

$$\mathbf{e}_l = \begin{pmatrix} 0 & 0 & 0 \\ 0 & 0 & 0 \\ 0 & 0 & 1 \end{pmatrix}. \tag{3.10d}$$

Even though they are very intuitive from a geometric point of view, they present some problems when we try to study them in depth: as an example of this we can see that the antenna pattern of the b and l is degenerate, i.e. it is the same unless for a multiplication constant. To understand why these polarizations present such a feature, we have to study in depth the properties of these polarizations.

In group theory, the 3x3 matrix with respect to the rotation operator has the $1 \oplus 3 \oplus 5$ irreducible subgroups:

- the trace that does not transform under rotation, which represents a spin 0 particle;
- the anti-symmetric part that transforms as once the rotation angle and, thus, represents a spin 1 particle;
- the symmetric part that transforms as twice the rotation angle and, thus, represents a spin 2 particle.

Since we are studying a metric theory, the anti-symmetric part does not exist, then the 6 components we have are actually the spin 0 particle and the 5 spin configurations of a spin 2 particle. This part is enough to explain the degeneracy of the antenna patterns of b and l polarization, in fact both these polarizations are a superposition of the spin 0 particle and of a spin 2 particle. However, since in the long wavelength approximation the detector measures the action of the wave on the different directions, the spin 0 component, which is a global expansion and contraction of the space, is not detectable. Thus, if we remove the trace from the matrices b and l, we obtain the same matrix less a multiplication constant.

For this reason, it would be better to use the d and t polarization instead of the b and

l. These new polarizations are,

$$\mathbf{e}_t = \begin{pmatrix} \frac{1}{3} & 0 & 0 \\ 0 & \frac{1}{3} & 0 \\ 0 & 0 & \frac{1}{3} \end{pmatrix}, \tag{3.11a}$$

$$\mathbf{e}_d = \begin{pmatrix} \frac{1}{3} & 0 & 0 \\ 0 & \frac{1}{3} & 0 \\ 0 & 0 & -\frac{2}{3} \end{pmatrix}. \tag{3.11b}$$

where the t polarization is the spin 0 particle, while the d (for diagonal) is a fifth spin 2 polarization.

Actually, the 5 polarizations obtained in this way can be adjusted with a normalization constant to make them comparable. The best way to obtain these constants is to build the 5 polarizations rotation eigenvectors. We can build these matrices using the rotation's ladder operators once we chose one direction for the spin calculation. Since we are considering the z axis as the propagation axis, we want to calculate the eigenvectors in respect to this axis. The ladder operator becomes $\hat{L}_\pm = \hat{L}_x \pm J\hat{L}_y$, where the $\hat{L}$ are the rotation generators

$$\hat{L}_{i(jk)} = \varepsilon_{i(jk)}, \tag{3.12}$$

where $\hat{L}_{i(jk)}$ are the j-th and k-th element of the i-th generator (where $i = 1,2,3$ correspond to $i = x,y,z$) and ε is the total anti-symmetric tensor. As is well known, the rotation ladder operator for a tensor is such that

$$\left[\mathbf{e}^l_m, L^+\right] = \sqrt{(l-m)(l+m+1)}\,\mathbf{e}^l_{m+1}, \tag{3.13a}$$

$$\left[\mathbf{e}^l_m, L^-\right] = \sqrt{(l+m)(l-(m-1))}\,\mathbf{e}^l_{m-1}, \tag{3.13b}$$

where $\mathbf{e}^l_m$ is the eigenvector with spin equals to l and spin-z equals to m. Since we are looking at spin 2 particles, we will omit the l value that is always 2. If we apply the L^- operator to the $m = -2$ eigenvector we obtain a null result. Starting from this, we can build the $m = -2$ GW matrix, that is

$$\mathbf{e}_{-2} = N\begin{pmatrix} 1 & -J & 0 \\ -J & -1 & 0 \\ 0 & 0 & 0 \end{pmatrix}, \tag{3.14}$$

where N is a normalization constant. Obviously $[\mathbf{e}_{-2}, L^z] = -2\mathbf{e}_{-2}$. Starting from this eigeivector, we can obtain all the others, increasing it with the + operator. Indeed, from (3.13a) we obtain

$$\mathbf{e}_{m+1} = \frac{\left[\mathbf{e}_m, L^+\right]}{\sqrt{(2-m)(3+m)}}; \tag{3.15}$$

from this result follow the remaining 4 eigenvectors:

$$\mathbf{e}_{-1} = N\begin{pmatrix} 0 & 0 & J \\ 0 & 0 & 1 \\ J & 1 & 0 \end{pmatrix}, \tag{3.16a}$$

$$\mathbf{e}_{0} = \sqrt{\frac{2}{3}}N\begin{pmatrix} 1 & 0 & 0 \\ 0 & 1 & 0 \\ 0 & 0 & -2 \end{pmatrix}, \tag{3.16b}$$

$$\mathbf{e}_{+1} = N\begin{pmatrix} 0 & 0 & J \\ 0 & 0 & -1 \\ J & -1 & 0 \end{pmatrix}, \tag{3.16c}$$

$$\mathbf{e}_{-2} = N\begin{pmatrix} 1 & J & 0 \\ J & -1 & 0 \\ 0 & 0 & 0 \end{pmatrix}, \tag{3.16d}$$

where N is the same for the 5 components and is a remaining normalization factor, and if we compute $[\mathbf{e}_m, L^z] = m\mathbf{e}_m$. This computation is essential if we want to normalize all the bases in the same way. The normalization used in GR is such that we have h_0 equal to 1, the $h_{\mathrm{DET}} = 1$, i.e.:

$$\mathbf{e}_{+} = \frac{1}{2}\begin{pmatrix} 1 & 0 & 0 \\ 0 & -1 & 0 \\ 0 & 0 & 0 \end{pmatrix}, \tag{3.17a}$$

$$\mathbf{e}_{\times} = \frac{1}{2}\begin{pmatrix} 0 & 1 & 0 \\ 1 & 0 & 0 \\ 0 & 0 & 0 \end{pmatrix}; \tag{3.17b}$$

in order to compare these polarizations with the spin-z eigenvectors we must apply a unit transformation to change one to another. The unit transformation we look for is

$$U(\theta) = \begin{pmatrix} \cos\theta & j\sin\theta & 0 \\ j\sin\theta & \cos\theta & 0 \\ 0 & 0 & 1 \end{pmatrix} \tag{3.18}$$

and if we apply this to $\mathbf{e}_+$ with an angle $\theta = -\pi/8$, we obtain

$$U^{+}(\theta)\mathbf{e}_{+}U(\theta) = \frac{\sqrt{2}}{2}\begin{pmatrix} 1 & -J & 0 \\ -J & -1 & 0 \\ 0 & 0 & 0 \end{pmatrix}. \tag{3.19}$$

From this we obtained $N = \sqrt{2}/2$ as the correct normalization to make the d component normalization coherent to the others. In that way, the correctly normalized d component is

$$\mathbf{e}_{d} = \sqrt{\frac{1}{3}}\begin{pmatrix} 1 & 0 & 0 \\ 0 & 1 & 0 \\ 0 & 0 & -2 \end{pmatrix}. \tag{3.20}$$

Once obtained the polarization basis, the last step is to define an elliptical polarization in this 5-dimensional-polarization space. Although using the spin eigenvalues might be more efficient for some scopes, we are going to use the same polarization that was used the previous studies, modified as we described above to have a one to one comparison. Thus the 5 polarizations we are going to use are the $\times$, $+$, x, y, d

We begin from the (A.16), and we start to collect coefficients in order to obtain something like (3.1). Moreover, it would be useful to have coefficients that express how far we are from the GR scenario. The more efficient procedure is to work on each spin group separately.

$+$ and $\times$ polarizations We already presented what the complex coefficients are in section 3.1, and we will use the same coefficients in order to keep the same form in the GR case. We might observe that if we have a GR polarization and we perform a rotation $R_z(\theta)$ along the propagation axis z, the $+$ and the $\times$ polarization will mix with a 2θ angle, according to the fact that these polarizations are the ones with | spin-z | = 2. For this reason, we will rename h_2 and $h_2(t)$ the h_0 and $h(t)$ respectively in (3.1) and will be a part of our overall polarization. The final form of this part of the polarization ellipse is

$$h_2(t) = h_2(H_+\mathbf{e}_+ + H_\times\mathbf{e}_\times)\mathrm{e}^{J\omega(t)t+\Phi_0}. \tag{3.21}$$

x and y polarizations Following the same pattern we used for the GR polarization, we can define the following component

$$h_1(t) = h_1(H_x\mathbf{e}_x + H_y\mathbf{e}_y)\mathrm{e}^{J\omega(t)t+\Phi_1}. \tag{3.22}$$

where complex components

$$H_x = \frac{\cos(\phi) - J\zeta\sin(\phi)}{\sqrt{1+\zeta^2}}, \tag{3.23a}$$

$$H_y = \frac{\sin(\phi) - J\zeta\cos(\phi)}{\sqrt{1+\zeta^2}}, \tag{3.23b}$$

are normalized to 1 (i.e.: $|H_x|^2 + |H_y|^2 = 1$), where ϕ is the angle defining the direction of the major axis of this sub-ellipse with respect to the celestial parallel, and ζ is the ratio between the major and the minor semi-axis of this sub-ellipse. It is also evident that with a rotation $R_z(\theta)$ along the propagation axis z, the x and the y polarization will mix with a θ angle, according to the fact that these polarizations are the ones with | spin-z | = 1.

d polarization As explained above, the d polarization is the one with spin-z= 0, that means that the basis $\mathbf{e}_d$ is alone and the complex components are just the module h_0 and the phase $\mathrm{e}^{J\Phi_2}$

$$h_0(t) = h_0\mathbf{e}_d\mathrm{e}^{J\omega(t)t+\Phi_2}. \tag{3.24}$$

The polarization ellipse To obtain the polarization ellipse, we finally sum the 3 components we obtained in the previous paragraphs, gaining the signal form as

$$\begin{aligned} h(t) &= h_2(t) + h_1(t) + h_0(t) = \\ &= h_2(H_+\mathbf{e}_+ + H_\times\mathbf{e}_\times)e^{J\omega(t)t+\Phi_0} + h_1(H_x\mathbf{e}_x + H_y\mathbf{e}_y)e^{J\omega(t)t+\Phi_1} + h_0\mathbf{e}_d e^{J\omega(t)t+\Phi_2}. \end{aligned} \tag{3.25}$$

We can now collect a global phase, that will be Φ_0 so that is the same phase as the GR scenario, and a global amplitude that we want to be the overall amplitude of the signal $h = \sqrt{h_0^2 + h_1^2 + h_2^2}$. As this is a kind of radius of a 3D sphere, we can express the h_i with polar coordinates

$$h_0 = h\sin\sigma\cos\tau, \tag{3.26a}$$
$$h_1 = h\sin\sigma\sin\tau, \tag{3.26b}$$
$$h_2 = h\cos\sigma, \tag{3.26c}$$

where σ represent how far we are from a GR signal, where 0 means that we have a GR signal and $\pi/2$ means that we have a completely non GR signal; τ is instead an angle showing the part of the signal has spin-z= 0. The final polarization form is the following

$$\begin{aligned} h(t) = h\big[&\cos\sigma(H_+\mathbf{e}_+ + H_\times\mathbf{e}_\times) + \sin\sigma\sin\tau(H_x\mathbf{e}_x + H_y\mathbf{e}_y)e^{J\epsilon_1} + \\ &+ \sin\sigma\cos\tau\mathbf{e}_d e^{J\epsilon_2}\big]\, e^{J\omega(t)t+\Phi_0}, \end{aligned} \tag{3.27}$$

where the new parameters $\epsilon_i = \Phi_i - \Phi_0$ with $i = 1,2$.

3.3 Non-GR Polarization Detector response

The last step is both to introduce non-GR signals in the simulations and to detect any non-GR signal. The procedure to follow is the same presented in [23] and showed in section 3.1, and we replace the basis tensor $\mathbf{e}_p$ with the detector response to that specific basis A_p, that is $\sum_{k=-2}^{2} A_k^p$. The result of the rotations gives us this series of response coefficients, to combine as described in (3.5)

5-vectors x

$$a_0^x = 0, \tag{3.28a}$$
$$a_{1c}^x = \sin(2a)\cos(\lambda)\sin(\delta), \tag{3.28b}$$
$$a_{1s}^x = -\frac{1}{2}\cos(2a)\sin(2\lambda)\sin(\delta), \tag{3.28c}$$
$$a_{2c}^x = -\sin(2a)\cos(\delta)\sin(\lambda), \tag{3.28d}$$
$$a_{2s}^x = \frac{1}{4}\cos(2a)\cos(\delta)(3-\cos(2\lambda)). \tag{3.28e}$$

5-vectors y

$$a_0^y = -\frac{3}{8}\cos(2a)(1+\cos(2\lambda))\sin(2\delta), \tag{3.29a}$$

$$a_{1c}^y = \frac{1}{2}\cos(2a)\sin(2\lambda)\cos(2\delta), \tag{3.29b}$$

$$a_{1s}^y = \sin(2a)\cos(\lambda)\cos(2\delta), \tag{3.29c}$$

$$a_{2c}^y = \frac{1}{8}\cos(2a)(3-\cos(2\lambda))\sin(2\delta), \tag{3.29d}$$

$$a_{2s}^y = \frac{1}{2}\sin(2a)\sin(\lambda)\sin(2\delta). \tag{3.29e}$$

5-vectors diagonal

$$a_0^d = -\frac{\sqrt{3}}{12}\cos(2a)(1-3\cos(2\delta))(1+\cos(2\lambda)), \tag{3.30a}$$

$$a_{1c}^d = \frac{\sqrt{3}}{3}\cos(2a)\sin(2\delta)\sin(2\lambda), \tag{3.30b}$$

$$a_{1s}^d = \frac{2\sqrt{3}}{3}\sin(2a)\sin(2\delta)\cos(\lambda), \tag{3.30c}$$

$$a_{2c}^d = -\frac{\sqrt{3}}{12}\cos(2a)(1+\cos(2\delta))(3-\cos(2\lambda)), \tag{3.30d}$$

$$a_{2s}^d = -\frac{\sqrt{3}}{3}(1+\cos(2\delta))\sin(2a)\sin(\lambda). \tag{3.30e}$$

This complete set of coefficients A_k^p is a matrix $\mathbb{R}^5 \to \mathbb{R}^5$ from the polarization space to the 5vector space. The determinant of the matrix is in general not null. This means that the matrix is generally revertible and any 5vector can be interpreted as a GW signal without, even the noise. This fact make us need a second unrelated detector to verify if we have the same waveform on both detectors and we have a real signal or not. This 10vector idea will be presented in the further section.

3.4 Non-GR detection with GR pipeline

The first step to justify the necessity of developing a Non-GR pipeline is to study what happens when we perform a standard GR search for a non GR signal. A set of tests have been done on the Hanford detector for the O1 dataset[5, 17], in order to understand how many non-GR signals would be detected by the GR pipeline. The tests have been done with an injection with some fixed parameters ($\alpha = 156.1318°$, $\delta = 39.6193°$ the right ascension and declination of the star; a frequency of 148.10Hz; a spindown of $-8.9782e-11$Hz/s; $\eta = 0.3549$; $\psi = 9.0961°$; $\zeta = 0.2768$; $\phi = 342,93°$; $\epsilon_1 = 263.4784°$; $\epsilon_2 = 73.6424°$), varying the σ and τ parameters and the amplitude h_0. The σ and τ parameters are selected so that sin of each angle spans the values between 0 and 1 with a step of 0.05. The h_0, instead, has the following values $[500, 50, 10, 9, 8, 7, 6, 5, 4, 3, 2, 1] \times 10^{-26}$, in a frequency where the Wiener Power spectrum of the noise is 7×10^{-27}.

From the results (e.g figure 3.1), it appears evident that the p value of the signal drops as σ angle increases, but if the GR signal is detected, most of the non-GR variants

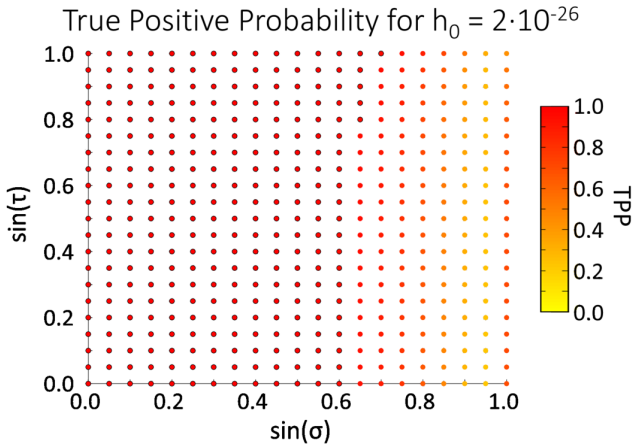

Figure 3.1. True positive probability for a signal with amplitude $h_0 = 2 \times 10^{-26}$, varying the σ and τ angles. The blue circled points are those whit True Positive Probability ≥ 95%.

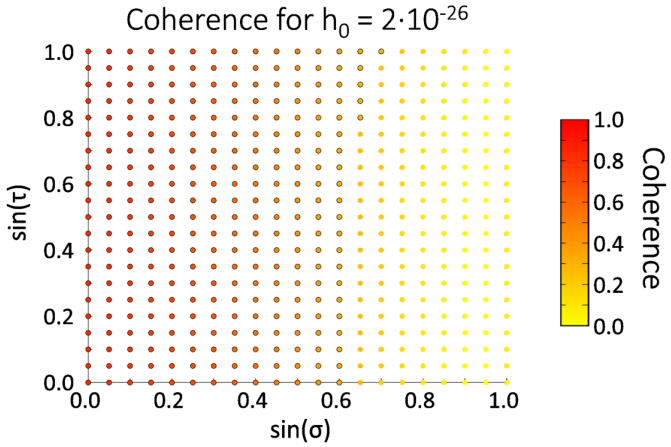

Figure 3.2. Coherence between the waveform of the signal and the one coming from the analysis. 1 represents a perfect match, while 0 is a complete wrong waveform. The blue circled points are those whit True Positive Probability ≥ 95%.

are detected. Anyway, it is also evident that the wave shape recovered by the standard pipeline is not correct, and the matched filter with the obtained wave shape does not match completely the signal (e.g. 3.2).

If we suppose that we are in a slightly non-GR universe (i.e. the universe is mostly GR and the non GR component σ is small), and since the non-GR detection is faster and more precise (we have 2 complex parameters to detect instead of 5 complex from the non-GR search), we can suppose to perform a standard GR search to detect a signal and then perform a non-GR one to improve the detected waveform.

3.5 Non-GR pipeline proposal

The last step is to understand how to implement a non-GR version of the search. As we saw in the previous paragraphs, we have 5 polarizations that are (in general) a complete

basis for the 5vector space, thus the first step is to increase the dimension of the analyzed space. Obviously, we cannot just add 2 dimensions to the actual space, for example by making $k \in [-3,3]$, since GW polarizations act on the 5 dimension complete space $k \in [-2,2]$ and the incremented space does not give us information on the noise part of the detector signal.

The way to increase the dimension of our space is to use more than one detector to extract the correlated signal, thus if our 5vector $\mathbb{X} \in \mathbb{D} \equiv \mathbb{C}^5$, where $\mathbb{D}$ is a single detector 5vector space, we can define a 5Nvector $\mathbb{Y} \in \mathbb{D}^N$ as a 5N component vector containing the 5vectors of each detector. Since the detectors response must be correlated, the uncorrelated part is due to noise, then we have 5 GW components and $5(N-1)$ components for the noise.

There are many strategies to define such a 5 dimension non-GR GW sub-basis from the 5N bases, but the more convenient approach is to select each of the 5 frequencies in each detector as a basis: in fact we will show how to build GW matrix starting from these bases.

Let's take the detector response to a generic h as in [23], rewritten in our coordinate system α, δ as right ascension and declination, λ as the detector's latitude and a the detector's azimuth. We can write the detector response as

$$x = \vec{u} \cdot h_{\mathrm{DET}} \cdot \vec{u} - \vec{v} \cdot h_{\mathrm{DET}} \cdot \vec{v}, \tag{3.31}$$

where $\vec{u} = (1\,0\,0)$ and $\vec{v} = (0\,1\,0)$ are the detector unitary arms in the detector frame and h_{DET} is the wave matrix in the same frame, that can be obtained through rotations of the h in the source frame as follows:

$$h_{\mathrm{DET}} = \mathbf{R}_3^T \mathbf{R}_2^T(t) \mathbf{R}_1^T \; h \, \mathbf{R}_1 \mathbf{R}_2(t) \mathbf{R}_3, \tag{3.32}$$

where the rotation operators are

$$\mathbf{R}_1 = R_z(\psi) R_x(\delta + \pi/2), \tag{3.33a}$$
$$\mathbf{R}_2(t) = R_z(-\Omega_{\mathrm{rot}} t - \alpha - \pi/2), \tag{3.33b}$$
$$\mathbf{R}_3 = R_y(\lambda + \pi/2) R_z(-a), \tag{3.33c}$$

and the $pi/2$ factors belong to the coordinate definitions. From (3.32), we can see that the time dependency (and consequently the frequency shift) belongs from $\mathbf{R}_2(t)$, while the other components, not depending on time, are just bases shuffling components.

Let's now write the polarization matrix in the earth reference frame (such that the z axis is the earth rotation axis), that is

$$h_\odot = \mathbf{R}_3^T h \mathbf{R}_3 = \sum_{p=-2}^{2} h_p \mathbf{e}_\odot^p \mathrm{e}^{-J(\omega t + \Phi)}, \tag{3.34}$$

where the h_p are the complex polarization parameters. If we now apply the earth rotation $\mathbf{R}_2(t)$ (where we included also α that will become a phase factor) we obtain the following result

$$\mathbf{R}_2^T(t)h_\odot\mathbf{R}_2(t) = \sum_{p=-2}^{2} h_p\mathbf{R}_2^T(t)\mathbf{e}_\odot^p\mathbf{R}_2(t)\mathrm{e}^{-\jmath(\omega t+\Phi)} =$$

$$= \sum_{p=-2}^{2} h_p\mathbf{R}_2^T(t)\mathbf{e}_\odot^p\mathbf{R}_2(t)\mathrm{e}^{-\jmath[\omega t+p(-\Omega_\odot t-\alpha-\pi/2)+\Phi]} = \tag{3.35}$$

$$= \sum_{p=-2}^{2} h_p\mathbf{R}_2^T(t)\mathbf{e}_\odot^p\mathbf{R}_2(t)\mathrm{e}^{-\jmath[(\omega+p\Omega_\odot)t+\Phi']},$$

that shows precisely how each of the $\mathbf{e}_p$ components goes to a specific frequency.

The last step is to rotate the earth reference frame to the detector frame and compute (3.31) for each $\mathbf{e}_\odot^p$ and call it E_p, the detector response to the p specific polarization:

$$E_p = \vec{u}\cdot\mathbf{R}_3^T\mathbf{e}_\odot^p\mathbf{R}_3\cdot\vec{u} - \vec{v}\cdot\mathbf{R}_3^T\mathbf{e}_\odot^p\mathbf{R}_3\cdot\vec{v}, \tag{3.36}$$

that result in the following

$$E_{-2} = \frac{N}{2}\cos(2a)[3-\cos(2\lambda)] + \jmath N\sin(2a)\sin(\lambda), \tag{3.37a}$$
$$E_{-1} = -\jmath N\cos(2a)\sin(2\lambda) + 2\sin(2a)\cos(\lambda), \tag{3.37b}$$
$$E_0 = -\sqrt{\frac{3}{2}}N\cos(2a)(1+\cos(2\lambda)), \tag{3.37c}$$
$$E_{+1} = -\jmath N\cos(2a)\sin(2\lambda) - 2\sin(2a)\cos(\lambda), \tag{3.37d}$$
$$E_{+2} = \frac{N}{2}\cos(2a)[(3-\cos(2\lambda)] - \jmath N\sin(2a)\sin(\lambda). \tag{3.37e}$$

Using these results, we can obtain the expected detector results as follows:

- compute the detector 5N data vector
- compute the polarization 5N response vector
- compute the earth-reference-frame GW matrix
- compute the source reference frame GW matrix.

Compute the detector 5Nvector data This first step is the same as the one in the original pipeline. For every detector (e.g. Livingston, Hanford, Virgo) we compute $\mathbb{X}_D$ as in (3.8). Once we have all the 5vectors from the dataset, we compute the 5N vectors, just by merging together the N computed 5 vectors:

$$\mathbb{Y} = (\mathbb{X}_{D_1} \ldots \mathbb{X}_{D_N}). \tag{3.38}$$

Compute the 5Nvector response For a chosen polarization p, the response 5vector for a specific detector $\mathbb{E}_p^D$ is a 5vector with all 0s but a the $3+p$ component (i.e. the first component for $p=-2$, the second for $p=-1$, ...) that is equal $E_p^{D_n}$, where the D refers to the detector, as the response is a function of λ and a that are detector dependent parameters. In that way we have the following 5 response 5vectors for the i-th detector

$$\mathbb{E}_{-2}^{D_i} = (E_{-2}(\lambda_{D_i}, a_{D_i})\ 0\ 0\ 0\ 0), \tag{3.39a}$$
$$\mathbb{E}_{-1}^{D_i} = (0\ E_{-1}(\lambda_{D_i}, a)\ 0\ 0\ 0), \tag{3.39b}$$
$$\mathbb{E}_{0}^{D_i} = (0\ 0\ E_0(\lambda_{D_i}, a_{D_i})\ 0\ 0), \tag{3.39c}$$
$$\mathbb{E}_{+1}^{D_i} = (0\ 0\ 0\ E_{+1}(\lambda_{D_i}, a_{D_i})\ 0), \tag{3.39d}$$
$$\mathbb{E}_{+2}^{D_i} = (0\ 0\ 0\ 0\ E_0(\lambda_{D_i}, a_{D_i})). \tag{3.39e}$$

If we want to build the response 5Nvector, we need to merge together the N computed 5vector response for a specific polarization p, i.e.

$$\mathbb{E}_p = (\mathbb{E}_p^{D_1} \dots X_p^{D_N}). \tag{3.40}$$

It is important to stress that the bases are orthogonal. Hence, we do not need to worry about correlations in the scalar products in the next steps.

Compute the earth-reference-frame GW matrix As in the GR case, since we do not have any information on the polarization form, we can estimate each of the 5 complex polarization values h_p as

$$\hat{h_p} = \frac{\mathbb{X} \cdot \mathbb{E}_p}{\mathbb{E}_p \cdot \mathbb{E}_p}; \tag{3.41}$$

this normalized scalar product can be used to build GW matrix in the earth-reference-frame $h_\odot$ as in (3.34).

Compute the source reference frame GW matrix The last step in order to obtain the matrix in the source frame (where the z axis is the wave propagation axis), is to perform back the $\mathbf{R}_3$ operator. Since the $\mathbf{R}_3$ is an orthogonal operator, the inverse one is actually the transposed, thus

$$\hat{h} = \mathbf{R}_3 h_\odot \mathbf{R}_3^T = \mathbf{R}_3 \left(\sum_{p=-2}^{2} \hat{h}_p \mathbf{e}_\odot^p \mathrm{e}^{-J(\omega t + \Phi)} \right) \mathbf{R}_3^T. \tag{3.42}$$

In that way we have reconstructed a generic polarization from the signal waveform in the detector.

Chapter 4

Conclusion

In this thesis we showed two improvement for the detection of GWs.

For the all-sky searches, we showed how to use the underlying data correlations to improve the searches. We widely used pattern recognition tools to find and extract the information in the dataset. The resulting pipeline improves the existing one, reducing by the 50% the number of candidates to follow up, without removing significant (injected) signals. This allows us to make deeper searches changing the kept number of candidates from the ranking procedure or increasing the precision of the previous threshold (e.g: keeping more candidates from the standard FrequencyHough step). Moreover, the fact that each signal produces a pattern of candidates might allow us to cluster the pattern itself and find the parameters using two pattern-based clusters. Anyway, more studies are necessary to understand how to effectively apply this procedure.

For the non-GR signals, we presented the antenna pattern obtained from such a signal, a detection study with the GR pipeline trying to detect such a signal and a theoretical proposal for a new non-GR pipeline. The fact that the GR pipeline can actually detect with a small false positive probability a non-GR signal stresses how the 5vectors pipeline is actually capable to detect the greatest part of any CW signal incoming from a source. The non-GR pipeline, anyway, can be useful to completely characterize the polarization of a detected signal as test of GR and non-GR theories.

Appendix A

Appendix

A.1 Revolution Doppler Effect in ecliptic coordinates

It is well known that the Doppler effect for a moving detector is given by

$$f(t) = \left(f_0 + \dot{f}\,t\right)\left(1 - \frac{\vec{v}\cdot\hat{n}}{c}\right), \tag{A.1}$$

where $\vec{v}$ is the detector velocity, $(-\hat{n})$ corresponds to the direction of the signal and c is the speed of light. We assume GW velocity to be equal to c, and the detector velocity to be the sum of the Earth rotation and revolution speed of the Earth $\vec{v}_{\rm rot} + \vec{v}_{\rm rev}$. If we neglect the Earth rotation velocity (that is $\sim 10^{-2} v_{\rm rev}$), and consider the Earth orbit as circular, we can easily express (A.1) in a very compact way using the geocentric ecliptic sky coordinates. In this coordinate system we can express the Sun position as

$$\vec{R}_{\rm S} = R_{\rm SE}\left[\cos(\Omega_{\rm rev}\,t),\ \sin(\Omega_{\rm rev}\,t),\ 0\right], \tag{A.2}$$

where $t = 0$ s is at the vernal equinox on the Northern Hemisphere, and $\Omega_{\rm rev}$ is the revolution angular velocity of the Earth. As a consequence, the Earth position with respect to the Sun is $\vec{R}_{\rm E} = -\vec{R}_{\rm S}$. We can use it to compute the Earth revolution velocity performing the time derivative of the Earth position with respect to the Sun, *i.e.*:

$$\vec{v}_{\rm rev} = \frac{\mathrm{d}}{\mathrm{d}t}\vec{R}_{\rm E} = -R_{\rm SE}\Omega_{\rm rev}\left[-\sin(\Omega_{\rm rev}\,t),\ \cos(\Omega_{\rm rev}\,t),\ 0\right]. \tag{A.3}$$

If we now consider a generic direction in the sky, $\hat{n} = (\cos\beta\cos\lambda,\ \cos\beta\sin\lambda,\ \sin\beta)$, and we solve the scalar product in (A.1), we obtain

$$f(t) = \left(f_0 + \dot{f}\,t\right)\left[1 + \frac{v_{\rm rev}}{c}\cos\beta\sin(\lambda - \Omega_{\rm rev}\,t)\right], \tag{A.4}$$

where we used $v_{\rm rev} = R_{\rm SE}\,\Omega_{\rm rev}$.

A.2 Hough Transform

The Hough Transform is a robust parameter estimator for patterns. Used mainly in digital image transformation and pattern recognition, it has some application also in astrophysics [25] as the CW data analysis for the Virgo LIGO detectors.[20]

We will describe now the Hough Transform for linear patterns, although it can be easily generalized to any kind of hypersurfaces of some differentiable manyfold.

A linear pattern can be considered a collection of lines in a $\mathbb{R}^2$ space (with coordinates x and y), where each element of the pattern can be identified by a set of parameters by a one-one map f. The standard set of parameters is $(m,q) \in \mathbb{R}^2$ where each line is described by

$$y = mx + q. \tag{A.5}$$

Thus, we have a function that maps a point of the parameter space (m,q) to a line in the original (x,y) space. Moreover, being a one-one function it can be easily inverted. We can observe that each point of the original space (x,y) is mapped to a line in the parameter space by the inverted function f^{-1}. If we have a set of points on the plane $\{P_i \equiv (x_i, y_i)\}$ that represents our observation, we can use this inverse function to project the points to the parameter space. If a linear pattern relation in a subset of the data points subsists, then in the parameter space the projected lines corresponding to the correlated points will intersect and the intersection coordinates will be the parameters which identify the correlation line.

This example represents a real observation situation where, because of the noise, not all the observations will be elements of the pattern, but we will have only a subset of them. Moreover, any two lines in the parameter space will intersect at some point (at most at infinity, if they are parallel). In this case, in order to detect a relevant line, we will assign to each intersection μ a number that is

$$n(\mu) = \sum_{\mu \in f^{-1}(P_c)} r_c \tag{A.6}$$

where r_c is a weight factor of the observation P_c. Usually the value of r_c is a constant 1, thus the n measurement (the /emphnumbercount) is the number of lines in the parameter space passing through the μ. Anyway, it might be useful to weight each point of the original plane P_c with some other known properties of the pattern. In the cases described in this thesis, since each observation has a detection statistic representing how likely is this candidate to be a real signal, we can use that parameter as weight.

Obviously, in a real experiment we don't have an infinite resolution on the plane (x,y), and each observation corresponds to a *plane* in the plane. Moreover, we will have some pixel discretization also in the parameter space that must be chosen so that the one-one relation still subsists: each pixel in the parameter space have to identify one and only one line in the original plane and vice versa.

Anyway, this discretization can create some approximation problems that reduce the numbercount on the correct line. For this reason, we need to split each pixel into sub-pixels to have a finer step. With this technique, each line will be described by a number of sub-pixels equals to the over-resolution factor (the number of sub-pixel in a pixel), so that this approximation effect is reduced. A simple case of this feature is shown in figure A.1.

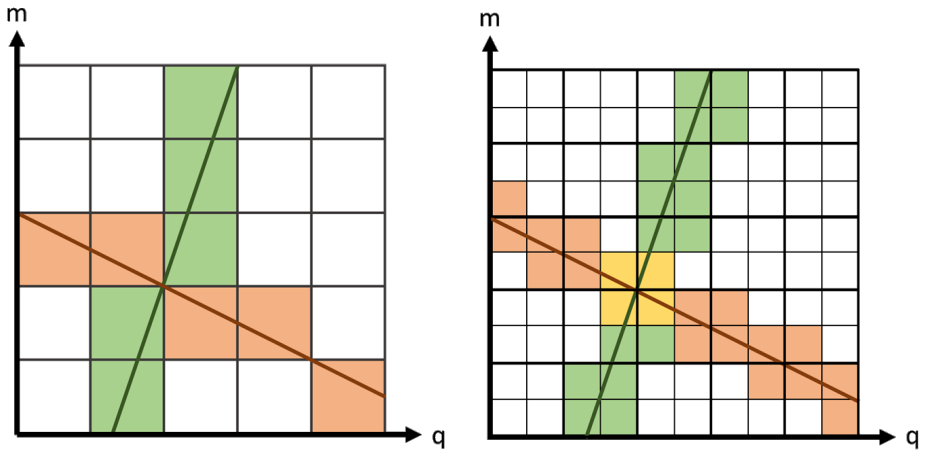

(a) Hough Transform **(b)** Hough Transform with over-resolution

Figure A.1. Hough example without and with the over-resolution. The red line votes the red cells; the green line votes the green cells. The yellow cells are voted by both lines. Without over-resolution there aren't yellow cells, while the over-resolution solves this problem.

A.3 Finding Λ

The following appendix describes how to find the value of Λ for a generic dataset.

The value of Λ has been found empirically by considering the Doppler-constant ρ curves, with ρ that is defined in (2.21). In the neighborhood of a signal we expect the highest numbercount candidates to accumulate on a specific F given by (2.24). We use this information and, for easiness, we consider a software injection with a strain amplitude $h_0 = 8 \times 10^{-25}$ at 108 Hz. We begin selecting all candidates coming from the FrequencyHough (0-Hough) transform for the whole sky within two times the maximum Doppler shift from the injection frequency, *i.e.*: $f \in [f_0(1-10^{-4}), f_0(1+10^{-4})]$. Then, we find what is the max numbercount (N_{noisy}) in a noisy region, which is taken far away from the injection frequency band, and we remove all candidates with numbercount smaller than N_{noisy}. Then, we compute $F(x) = \text{variance}_{\text{N}}(f + f\cos(\beta)\sin(\lambda - x)\frac{v_{\text{rev}}}{c})$, where f, β and λ are the coordinates of the candidates, while the $\text{variance}_{\text{N}}$ is the numbercount weighted variance computed on all candidates in the selected subset. The value of x that minimize $F(x)$ is a good value for Λ.

A.4 Computing cost model

In this section we present the computing cost associated to the new chain of vetoes. All times are intended as CPU times. The total computation cost for the analysis is

$$T = T_{\text{f-SkyHough}} + T_{\text{Clust}} + T_{\text{f-Skyveto}}, \tag{A.7}$$

where $T_{\text{f-SkyHough}}$ represents the computational cost needed to compute the frequency-sky Hough transform, T_{Clust} the computational cost needed to cluster the candidates

coming from the frequency-sky Hough transform and $T_{\text{f-Skyveto}}$ represents the computational cost to perform the whole Spindown-Sky veto.

$T_{\text{f-SkyHough}}$ scales linearly with the number of candidates. According to the FrequencyHough selection rule, the number of candidates (N_{c}) scales with the number of sky points N_{D} in the grid (as described in section 2.1.2), which in turn scales as the square of the frequency. Hence,

$$T_{\text{f-SkyHough}} = c_1 N_{\text{c}} = c_1 4\pi N_{\text{D}}^2 = c_1 4\pi \left(f\, T_{\text{FFT}} \frac{v_{\text{rev}}}{c} \right)^2, \tag{A.8}$$

where c_1 is a constant evaluated as 15×10^{-4} s and by timing the application.

T_{Clust} has been empirically measured to scale linearly with the frequency, *i.e.*:

$$T_{\text{Clust}} = c_2 f, \tag{A.9}$$

where c_2 is a constant evaluated as 0.10 s/Hz by simple timing.

The last component, $T_{\text{f-Skyveto}}$, is the time needed to perform a $\dot{f}$-sky Hough map on all clusters selected in the previous step. This variable depends on the number of candidates in every cluster and on the number of clusters for every frequency value:

$$T_{\text{f-Skyveto}} = N_{\text{clusters}}\, T_{\text{vetopercluster}}, \tag{A.10}$$

where $N_{\text{clusters}} = 2 \times 10^4$ is the number of clusters per Hz and $T_{\text{vetopercluster}} = c_3 \text{e}^{f\tau}$ is the time needed to apply the veto to every cluster, while $c_3 = 0.3$ s and $\tau = 0.1$ s are two constants obtained empirically.

As an example, the total computation time in (A.7) is 3 300 CPU hour for the vetoes applied on a single detector and using O2 data. We note that such computation time is small compared to the time needed for the standard Hough transform [12], while there is a significant gain in computational cost as regards the follow up of candidates, whose number is drastically reduced by the new vetoes presented here.

A.5 Elliptical polarization scheme for N polarizations

In this section we will present how to draw a generic elliptical polarization with a N items base of polarizations.

We will begin by showing how an ellipse can be described using 2 generating vectors $\vec{h}_1$ and $\vec{h}_2$. Then we will show how to use a compact complex notation, and finally how this notation will be useful to define a generic wave.

Ellipse in a 2-Dimension Euclidean space It can be shown how any ellipse is an *affine image* of the unit circle.

In order to show that, let's start by defining a parameter v and writing the parametric definition of unit circle in the Euclidean plan $\vec{x} = (\cos v, \sin v)$. Let's now define an affine transformation as $\vec{x} \to \vec{h}_0 + A\vec{x}$ where $\vec{h}_0$ is an arbitrary vector and A is an invertible matrix whose columns can be written as the vectors $\vec{h}_1$ and $\vec{h}_2$. Being invertible will consider (for now) that the vectors $\vec{h}_1$ and $\vec{h}_2$ cannot be parallel (since the determinant is not null). In that way the unit vector is mapped in an ellipse centred in $\vec{h}_0$ while $\vec{h}_1$ and $\vec{h}_2$ are the directions of two conjugate diameters (i.e: the diameter along $\vec{h}_1$ is bisected by the diameter along $\vec{h}_2$ and vice-versa).

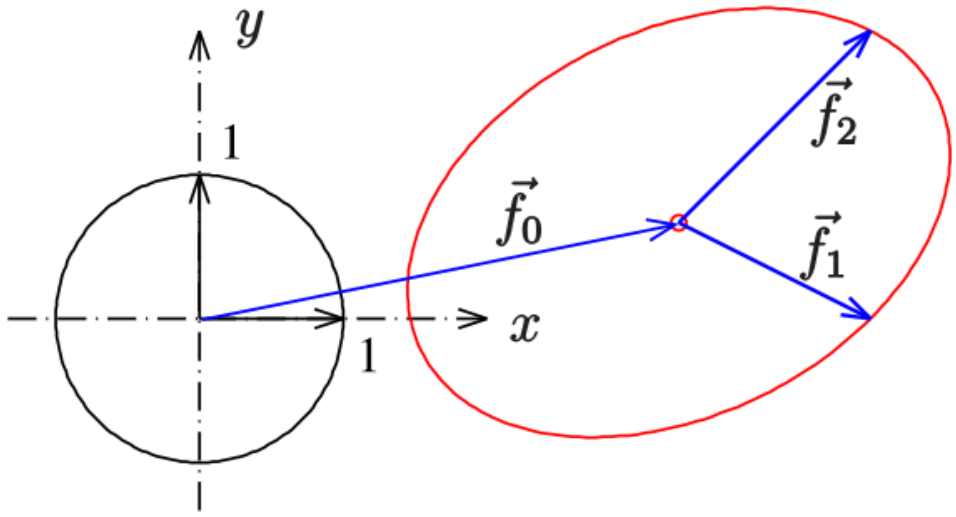

Figure A.2. Affine projection of an unit circle into an ellipse

Since the generating vectors are not perpendicular, the diameters that lay on those vectors are not the major and minor axes. If we want to find those axes, we can find the distance from the centre $d(v)$ and find the stationary points in the v parameter. The results give that the four vertices are the point obtained for $v = v_0 + \frac{k}{2}\pi$ where k goes from 0 to 3, and v_0 is defined by

$$\tan(2v_0) = \frac{2\vec{h}_1 \cdot \vec{h}_2}{\left|\vec{h}_1\right|^2 - \left|\vec{h}_2\right|^2}. \tag{A.11}$$

Since we don't need it, from now on we will consider $\vec{h}_0$ a null vector.

Parallel generating vectors By definition, if the determinant of A is null, we are projecting our 2D space in one 1D surface. In fact, in this case we can write $\vec{h}_2 = \alpha\vec{h}_1$, and the projection of the parametric unit circle becomes

$$\begin{aligned}
\vec{x}(u) &= \begin{pmatrix}\vec{h}_1\\ \vec{h}_2\end{pmatrix}\begin{pmatrix}\cos(u) & \sin(u)\end{pmatrix} = \\
&= \vec{h}_1\cos(u) + \vec{h}_2\sin(u) = \\
&= \vec{h}_1\cos(u) + \alpha\vec{h}_1\sin(u) = \\
&= \vec{h}_1\left(\cos(u) + \alpha\sin(u)\right) = \\
&= \vec{h}_1\sqrt{1+\alpha^2}\left(\frac{1}{\sqrt{1+\alpha^2}}\cos(u) + \frac{\alpha}{\sqrt{1+\alpha^2}}\sin(u)\right) = \\
&= \vec{h}_1\sqrt{1+\alpha^2}\left(\cos(\phi)\cos(u) + \sin(\phi)\sin(u)\right) = \\
&= \vec{h}_1\sqrt{1+\alpha^2}\ \cos(u-\phi)
\end{aligned} \tag{A.12}$$

where we have defined a new variable $\phi = \arctan(\alpha)$ which means that $\sin(\phi) = \frac{\alpha}{\sqrt{1+\alpha^2}}$ and $\cos(\phi) = \frac{1}{\sqrt{1+\alpha^2}}$.

This object clearly describes a line segment, and this is what we want, since we can think of a segment as an ellipse with the minor axis $b \equiv 0$. For this reason we can omit the hypothesis *AA invertible* we used in the previous paragraph.

Ellipse in an N-Dimension Euclidean space Let's work now in a $\mathbb{R}^N$ Euclidean space. We want still to define a 2D ellipse, starting with 2 vectors and performing a transformation $B : \mathbb{R}^2 \to \mathbb{R}^N$, while B is a $(N \times 2)$ matrix. We will then have 2 vectors ($\vec{h}_1$ and $\vec{h}_2$) with N components each. We also know that a 2D surface in a generic space can be defined as $P = \alpha\vec{h}_1 + \beta\vec{h}_2$, where α and β are generic real coefficient. Hence, we note that the surface P is exactly the one on which our ellipse lays, and if we apply the transformation B on the unit circle we have an ellipse.

Complex notation The last step we are doing is to pass from the real notation to a complex one in order to make it more compact. Let's consider our ellipse

$$\vec{x}(t) = \vec{h}_1 \cos(\lambda) + \vec{h}_2 \sin(\lambda); \tag{A.13}$$

this is a real equation, so we can take the real part of this equation without changing anything, but if we perform this operation we can add some imaginary part to the equation without consequences.

$$\begin{aligned} \vec{x}(t) &= \Re\left(\vec{h}_1 \cos(\lambda) + \vec{h}_2 \sin(\lambda)\right) = \\ &= \Re\left[\vec{h}_1 \left(\cos(\lambda) - \jmath \sin(\lambda)\right) + \vec{h}_2 \left(\sin(\lambda) + \jmath \cos(\lambda)\right)\right]. \end{aligned} \tag{A.14}$$

If we finally collect $\jmath$ in the $\vec{h}_2$ part, we can write our equation in a very compact form

$$\vec{x}(t) = \Re\left[\vec{h}_1 \left(\cos(\lambda) - \jmath \sin(\lambda)\right) + \jmath \vec{h}_2 \left(\cos(\lambda) - \jmath \sin(\lambda)\right)\right] = \Re\left[(\vec{h}_1 + \jmath \vec{h}_2) \mathrm{e}^{-\jmath\lambda}\right]. \tag{A.15}$$

Thus, as long as we remember to use only the real part, we can write the unity circle as a complex exponential times a complex vector $\vec{h} \equiv \vec{h}_1 + \jmath \vec{h}_2$.

Elliptical Polarization The last step is to project the ellipse from the Euclidean space to the polarization space, that is a simple scalar product between the complex coefficient vector $\vec{h}$ and the bases vector $\vec{\mathbf{e}}$, where each component is a base of GW matrix $\mathbf{e}_p$. In that way, we have

$$\vec{x} \cdot \vec{\mathbf{e}} = \Re\left(\sum_p h_p \mathbf{e}_p \mathrm{e}^{-\jmath\lambda}\right) \tag{A.16}$$

where λ is the wave phase.

A.6 Polarization extractor

The following section describes a series of operators to extract a specific polarization component from a generic matrix. This operator is useful both to change reference frame and to extract a polarization component from a specific GW polarization (e.g one coming from a specific theory). These operators are presented for the spin-z base from (3.14) and

(3.16), but it is quite easy to adjust them for the spin-x and spin-y bases, by just changing the indices.

We will describe the operator as $O_k(\mathbf{h})$, where $\mathbf{h}$ is GW matrix, $k \in [-2,2]$ is GW component with spin-z= k. The operator is designed such that $O_k(\mathbf{e}_m) = \delta_{km}$ where the $\mathbf{e}_m$ are the ones coming from (3.14) and (3.16). The operators O_k are

$$O_{-2}(\mathbf{h}) = \frac{h_{11} - h_{22} + \jmath h_{12} + \jmath h_{21}}{4N} \tag{A.17a}$$

$$O_{-1}(\mathbf{h}) = \frac{-\jmath h_{13} - \jmath h_{31} + h_{23} + h_{32}}{4N} \tag{A.17b}$$

$$O_0(\mathbf{h}) = \sqrt{\frac{3}{2}} \frac{h_{11} + h_{22} - h_{33}}{4} \tag{A.17c}$$

$$O_{-1}(\mathbf{h}) = \frac{-\jmath h_{13} - \jmath h_{31} - h_{23} - h_{32}}{4N} \tag{A.17d}$$

$$O_{+2}(\mathbf{h}) = \frac{h_{11} - h_{22} + \jmath h_{12} + \jmath h_{21}}{4N} \tag{A.17e}$$

where N is the normalization factor described in the 3.2.

Bibliography

[1] J. Aasi et al. “Advanced LIGO”. In: *Classical and Quantum Gravity* 32.7 (Mar. 2015), p. 074001. ISSN: 1361-6382. DOI: 10.1088/0264-9381/32/7/074001. URL: http://dx.doi.org/10.1088/0264-9381/32/7/074001.

[2] J. Abadie et al. “Beating the spin-down limit on gravitational wave emission from the Vela pulsar”. In: *Astrophys. J.* 737 (2011), p. 93. DOI: 10.1088/0004-637X/737/2/93. arXiv: 1104.2712 [astro-ph.HE].

[3] B. P. Abbott et al. “All-sky search for continuous gravitational waves from isolated neutron stars using Advanced LIGO O2 data”. In: *Phys. Rev.* D100.2 (2019), p. 024004. DOI: 10.1103/PhysRevD.100.024004. arXiv: 1903.01901 [astro-ph.HE].

[4] B. P. Abbott et al. “Observation of Gravitational Waves from a Binary Black Hole Merger”. In: *Phys. Rev. Lett.* 116.6 (2016), p. 061102. DOI: 10.1103/PhysRevLett.116.061102. arXiv: 1602.03837 [gr-qc].

[5] B. P. Abbott et al. “All-sky Search for Periodic Gravitational Waves in the O1 LIGO Data”. In: *Phys. Rev.* D96.6 (2017), p. 062002. DOI: 10.1103/PhysRevD.96.062002. arXiv: 1707.02667 [gr-qc].

[6] B. P. Abbott et al. “First search for nontensorial gravitational waves from known pulsars”. In: *Phys. Rev. Lett.* 120.3 (2018), p. 031104. DOI: 10.1103/PhysRevLett.120.031104. arXiv: 1709.09203 [gr-qc].

[7] F. Acernese et al. “Advanced Virgo: a second-generation interferometric gravitational wave detector”. In: *Classical and Quantum Gravity* 32.2 (Dec. 2014), p. 024001. ISSN: 1361-6382. DOI: 10.1088/0264-9381/32/2/024001. URL: http://dx.doi.org/10.1088/0264-9381/32/2/024001.

[8] P. Astone, S. Frasca, and C. Palomba. “The short FFT database and the peak map for the hierarchical search of periodic sources”. In: *Classical and Quantum Gravity* 22.18 (2005), S1197. URL: http://stacks.iop.org/0264-9381/22/i=18/a=S34.

[9] P. Astone et al. “Coherent search of continuous gravitational wave signals: extension of the 5-vectors method to a network of detectors”. In: *Journal of Physics: Conference Series* 363 (June 2012), p. 012038. DOI: 10.1088/1742-6596/363/1/012038. URL: https://doi.org/10.1088%2F1742-6596%2F363%2F1%2F012038.

[10] P. Astone, S. D’Antonio, S. Frasca, and C. Palomba. “A method for detection of known sources of continuous gravitational wave signals in non-stationary data”. In: *Class. Quant. Grav.* 27 (2010), p. 194016. DOI: 10.1088/0264-9381/27/19/194016.

[11] P. Astone, S. Frasca, and C. Palomba. “The short FFT database and the peak map for the hierarchical search of periodic sources”. In: *Class. Quant. Grav.* 22 (2005), S1197–S1210. DOI: 10.1088/0264-9381/22/18/S34.

[12] P. Astone, A. Colla, S. D’Antonio Sabrina and Frasca, and C. Palomba. “Method for all-sky searches of continuous gravitational wave signals using the frequency-Hough transform”. In: *Phys. Rev.* D90.4 (2014), p. 042002. DOI: 10.1103/PhysRevD.90.042002. arXiv: 1407.8333 [astro-ph.IM].

[13] C. Caprini et al. “Science with the space-based interferometer eLISA. II: gravitational waves from cosmological phase transitions”. In: *Journal of Cosmology and Astroparticle Physics* 2016.04 (2016), p. 001. URL: http://stacks.iop.org/1475-7516/2016/i=04/a=001.

[14] P. B. Covas et al. “Identification and mitigation of narrow spectral artifacts that degrade searches for persistent gravitational waves in the first two observing runs of Advanced LIGO”. In: *Phys. Rev.* D97.8 (2018), p. 082002. DOI: 10.1103/PhysRevD.97.082002. arXiv: 1801.07204 [astro-ph.IM].

[15] D. Eardley, D. Lee, and A. Lightman. “Gravitational-wave observations as a tool for testing relativistic gravity”. In: *Phys. Rev. D* 8 (1973), pp. 3308–3321. DOI: 10.1103/PhysRevD.8.3308.

[16] A. Einstein. “Über Gravitationswellen”. In: *Sitzungsber. Preuss. Akad. Wiss. Berlin (Math. Phys.)* 1918 (1918), pp. 154–167.

[17] *Gravitational Wave Open Science Center: O1 and O2 data sets. O1 covers the time period starting from September 12, 2015 up to January 19, 2016. O2 spans the time period from November 30, 2016, up to August 25, 2017.* https://www.gw-openscience.org.

[18] B. Haskell, L. Samuelsson, K. Glampedakis, and N. Andersson. “Modelling magnetically deformed neutron stars”. In: *Monthly Notices of the Royal Astronomical Society* 385.1 (Feb. 2008), pp. 531–542. ISSN: 0035-8711. DOI: 10.1111/j.1365-2966.2008.12861.x. URL: http://dx.doi.org/10.1111/j.1365-2966.2008.12861.x.

[19] R. Hulse and J. Taylor. “Discovery of a pulsar in a binary system”. In: *Astrophys. J. Lett.* 195 (1975), pp. L51–L53. DOI: 10.1086/181708.

[20] J. Illingworth and J. Kittler. “A survey of the Hough transform”. In: *Computer vision, graphics, and image processing* 44.1 (1988), pp. 87–116.

[21] G. Intini et al. “A Doppler-modulation based veto to discard false continuous gravitational-wave candidates”. In: *Classical and Quantum Gravity* (2020). URL: http://iopscience.iop.org/10.1088/1361-6382/abac43.

[22] M. Isi, A. J. Weinstein, C. Mead, and M. Pitkin. “Detecting beyond-Einstein polarizations of continuous gravitational waves”. In: *Phys. Rev. D* 91 (8 Apr. 2015), p. 082002. DOI: 10.1103/PhysRevD.91.082002. URL: https://link.aps.org/doi/10.1103/PhysRevD.91.082002.

[23] P. Jaranowski, A. Królak, and B. F. Schutz. “Data analysis of gravitational-wave signals from spinning neutron stars: The signal and its detection”. In: *Physical Review D* 58.6 (Aug. 1998). ISSN: 1089-4918. DOI: 10.1103/physrevd.58.063001. URL: http://dx.doi.org/10.1103/PhysRevD.58.063001.

[24] M. Kramer and N. Wex. “The double pulsar system: A unique laboratory for gravity”. In: *Class. Quant. Grav.* 26 (2009), p. 073001. DOI: 10.1088/0264-9381/26/7/073001.

[25] B. Krishnan et al. “The Hough transform search for continuous gravitational waves”. In: *Phys. Rev. D* 70 (2004), p. 082001. DOI: 10.1103/PhysRevD.70.082001. arXiv: gr-qc/0407001.

[26] S. Mastrogiovanni et al. “An improved algorithm for narrow-band searches of continuous gravitational waves”. In: *Classical and Quantum Gravity* 34.13 (June 2017), p. 135007. ISSN: 1361-6382. DOI: 10.1088/1361-6382/aa744f. URL: http://dx.doi.org/10.1088/1361-6382/aa744f.

[27] F. Özel and P. Freire. “Masses, Radii, and the Equation of State of Neutron Stars”. In: *Annual Review of Astronomy and Astrophysics* 54.1 (2016), pp. 401–440. DOI: 10.1146/annurev-astro-081915-023322. eprint: https://doi.org/10.1146/annurev-astro-081915-023322. URL: https://doi.org/10.1146/annurev-astro-081915-023322.

[28] C. Palomba, P. Astone, and S. Frasca. “Adaptive Hough transform for the search of periodic sources”. In: *Class. Quant. Grav.* 22 (2005), S1255–S1264. DOI: 10.1088/0264-9381/22/18/S39.

[29] B. F. Schutz. “Gravitational wave sources and their detectability”. In: *Classical and Quantum Gravity* 6.12 (Dec. 1989), pp. 1761–1780. DOI: 10.1088/0264-9381/6/12/006. URL: https://doi.org/10.1088%2F0264-9381%2F6%2F12%2F006.

[30] J. Taylor and J. Weisberg. “A new test of general relativity. Gravitational radiation and the binary pulsar PSR 1913+16”. In: *Astrophysucal Journal* (253 1982), pp. 908–920. DOI: 10.1086/159690.

[31] V.Ferrari and L. Gualtieri. “General Relativity”. 2010.